Geophysical Journal International

Geophys. J. Int. (2022) **230,** 813–830
Advance Access publication 2022 February 26
GJI Seismology

https://doi.org/10.1093/gji/ggac086

Crustal structure and intraplate seismicity in Nordland, Northern Norway: insight from seismic tomography

H.A. Shiddiqi,[1] L. Ottemöller,[1] S. Rondenay,[1] F. Halpaap,[1] S. Gradmann[2] and J. Michálek[1]

[1]*Department of Earth Science, University of Bergen,* 5007 *Bergen, Norway. E-mail: hasbi.shiddiqi@uib.no*
[2]*Geological Survey of Norway, Trondheim N-7491, Norway*

Accepted 2022 February 24. Received 2022 February 23; in original form 2021 December 1

SUMMARY

The Nordland region, Northern Norway, situated in an intraplate continental setting, has the highest seismicity rate in mainland Norway. However, the exact cause of seismicity in this region is still debated. Better understanding of factors that influence the seismicity in Nordland can help increase knowledge of intraplate seismicity in general. Here, we address this problem with the aid of a new high-resolution 3-D V_P and V_P/V_S ratio images of the crust in Nordland using seismic traveltime tomography. These images show the existence of a localized, 10–15 km Moho step that runs parallel to the coast. The north–south extent of this step coincides with the region that exhibits the highest rates of seismicity. Focal mechanisms of selected earthquakes computed in this study are dominated by normal and oblique-normal, indicating a coast-perpendicular extension. The coast-perpendicular extensional stress regime deviates from the regional compression imposed by the ridge push from the North Atlantic. This deviation is thought to stem from the additional interference with local flexural stress caused by sediment redistribution and glacial isostatic adjustment, and possibly exacerbated by gravitational potential energy stress associated with the Moho step. The deformation due to the extensional regime is localized on pre-existing faults and fractures along the coastline. The tomography result shows that two distinct seismic swarms occurred in the coastal area with low V_P and variable V_P/V_S ratio anomalies, pointing towards fractured crust and possibly the presence of fluids. The existence of fluids here can change the differential stress and promote seismic rupture.

Key words: Europe; Body waves; Crustal imaging; Seismic tomography; Intraplate processes.

1 INTRODUCTION

Intraplate earthquakes occur within stable continental regions away from the plate boundaries. Many of these events occur within reactivated ancient rift systems or continental passive margins (Schulte & Mooney 2005). This general framework applies to Norway, which has a low-to-moderate rate of intraplate seismicity. Here, seismicity is highest along the shelf edge, in the North sea, and along the coast. The largest known earthquake to have affected the region is the 1819, M 5.9 earthquake, which occurred in Lurøy, Nordland, Northern Norway (Muir-Wood 1989; Bungum & Olesen 2005; Måntyniemi *et al.* 2020).

The Nordland region, which extends between 66°N and 69°N and includes the Lofoten-Vesterålen islands (Fig. 1), is an example of a seismically active intraplate setting where various sources of intraplate stress interact in a relatively small region. The offshore area of Nordland is a rifted passive margin, whereas the mainland area comprises the remainders of the Scandinavian Caledonides, which includes the high topography region of the northern Scandes mountains.

Investigating the crustal structure of passive margins can improve our understanding of the causes of seismicity in these tectonic settings. However, since many regions are still monitored by sparse seismic networks, providing a better 3-D crustal structure remains a challenge. This is also the case for the Nordland region as a whole—to date, only the offshore region, for example the Lofoten-Vesterålen margin, has been mapped in detail by deep seismic surveys (e.g. Mjelde *et al.* 1993, 1998; Breivik *et al.* 2017).

In this study, we investigate the generating mechanism of intraplate seismicity in the Nordland region. We made use of permanent and recent temporary seismic networks to develop a 3-D seismic velocity model using seismic traveltime tomography. In addition, we determined the focal mechanisms using the 3-D velocity model. The resulting velocity model gives insight into the complex

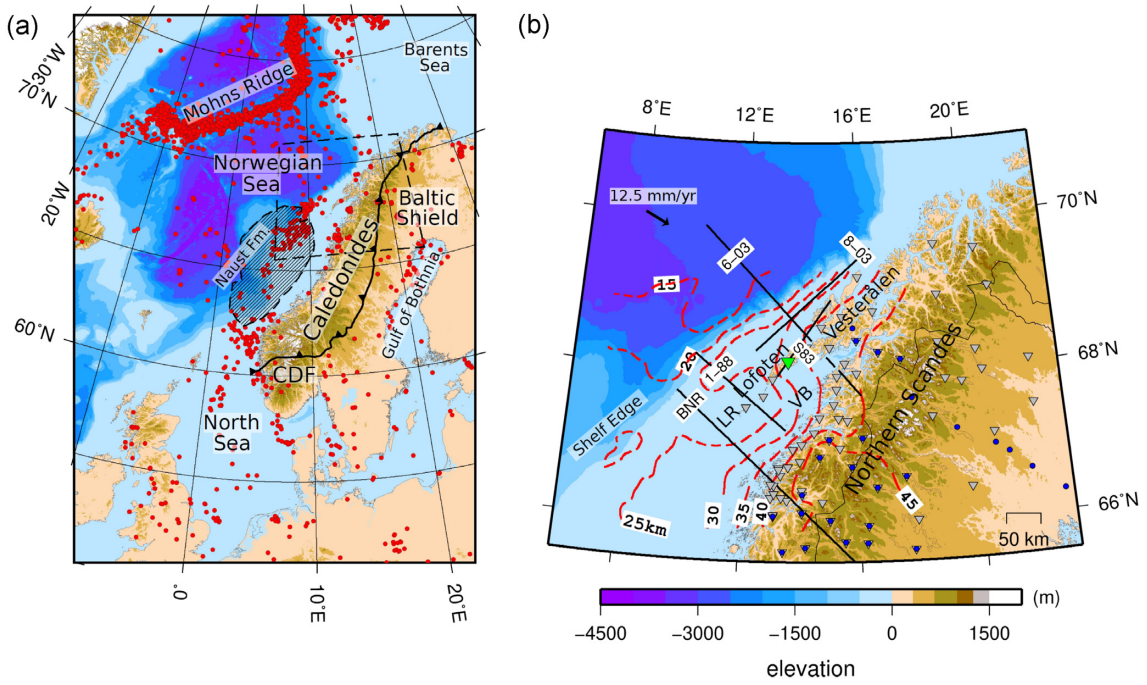

Figure 1. (a) The map of major tectonic features in the region encompassing Fennoscandia and the North Atlantic regions along with the distribution of earthquakes ($M \geq 3$) (red circles) for the period of 1990–2020 obtained from the National Norwegian Seismic Network catalogue. The dashed rectangle is the study region shown in Fig. 1(b). The Naust formation (Naust Fm.) is shown as black stripes area. LR, Lofoten Ridge; VB, Vestfjorden Basin; JMFZ, Jan Mayen Fracture Zone; SFZ, Senja Fracture Zone; CDF, Caledonian Deformation Front. The study area is shown as the dashed box. (b) Map of Nordland and the surrounding region. Contours of Moho depth (in km) from Maystrenko *et al.* (2017) are shown as red dashed lines. Plate velocity relative to the North American Plate (shown as black arrow) obtained from ITRF 2014 model (Altamimi *et al.* 2016). Bathymetry and topography data are obtained from SRTM15+ (Tozer *et al.* 2019). Seismic stations used in this study are shown as grey reverse triangles. Station LOF is depicted as blue reverse triangle. Stations used by Ben-Mansour *et al.* (2018) to obtain Moho depth using receiver function method are depicted by blue circles. Deep seismic profiles mentioned in the text are shown as black solid lines.

crustal structure and composition of the region. Finally, we considered together the 3-D velocity models and the focal mechanism solutions to explore the relation between the crustal structure and the intraplate seismicity in Nordland. Knowledge obtained in this study will not only improve our ability to assess the hazards posed by Nordland earthquakes but it may also help better understand the cause of seismicity in other similar passive margin environments.

2 BACKGROUND

Here, we summarize the tectonic setting and provide a simplified geological overview of the study area. Then, we describe the state of the art for geophysical constraints on the crustal structure of Nordland. In the last part of this section, we highlight the main tectonic forces that influence the present day stress field, and reiterate the hypotheses regarding the causative mechanism of intraplate seismicity in Nordland from previous studies.

2.1 Tectonic setting of Nordland

The Nordland region comprises the high topography of the Northern Scandes to the east and the Lofoten-Vesterålen margin, which is part of the Mid-Norwegian margin, to the west (Fig. 1). The region is part of the Caledonian domain, affected by the late stages of collision of Baltica and Laurentia (Corfu *et al.* 2014). Following the collapse of the Caledonian orogen in the Devonian, the Mid-Norwegian margin was formed through several tectono-magmatic stages (Tsikalas *et al.* 2001; Faleide *et al.* 2008). The long phases of extension and rifting culminated in the continental breakup and opening of the Atlantic in the Early Eocene. The continental breakup was followed by the formation of the North Atlantic Igneous Province and the Norwegian margin (see e.g. Eldholm & Grue 1994; Horni *et al.* 2017).

The narrow Lofoten-Vesterålen margin is located between the Senja Fracture zone to the north and the Vøring margin to the south, and marked by the exposed Lofoten-Vesterålen islands. The islands comprises the exposed Archean and Proterozoic basement [National bedrock database, Geological Survey of Norway (2011)]. Between the Lofoten islands and the Norwegian mainland lies the Vestfjorden basin with a basement depth ranging from 6 to 10 km (Brönner *et al.* 2013; Maystrenko *et al.* 2017).

The Nordland area is dominated by a stack of nappe complexes formed as a result of the collision. Nordland is mostly covered by the upper and the uppermost Allochton (Corfu *et al.* 2014). During the late Caledonian era, several extensional shear zones formed along the Caledonian domain with WSW–ENE directions in central and northern Norway (Fossen 2010). These shear zones appear to extend down into the basement, in some cases reaching the deeper part of the crust (Fossen 2010). Major shear zones in Nordland include the Sagfjord shear zone in the north, and the Nesna shear zone in the south, which extends further offshore and is connected to the Bivrost lineament (Fig. 2).

During the Late Pliocene and Pleistocene, Scandinavia underwent several sequences of deglaciation and erosion, which deposited large volumes of sediments offshore (Rise *et al.* 2005). The Naust formation located along the Mid-Norwegian margin (between 62°N

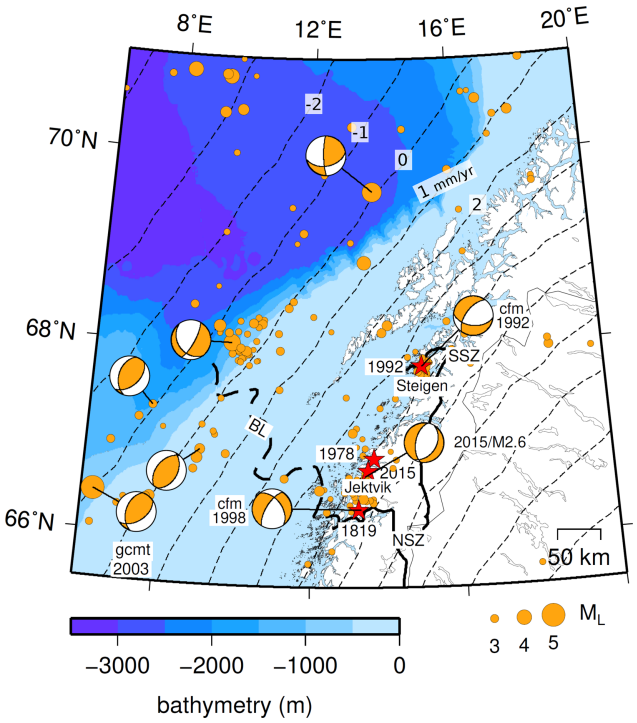

Figure 2. Seismicity in the study region from NNSN catalogue for the period of 1980–2019 ($M \geq 2.5$) shown as orange circles. Red stars depict the notable seismic events in the coastal area of Nordland: 1819 Lurøy earthquake, and three series of seismic swarms mentioned in the text. Focal mechanism of offshore events are obtained from Bungum *et al.* (1991), except for the 2003 M_w 5.1 event obtained from global CMT catalogue (labelled as 'gcmt 2003', Ekström *et al.* 2012). Composite focal mechanisms labelled with 'cfm' labels are obtained from Hicks *et al.* (2000a) for the 1998 solution, and from Atakan *et al.* (1994) for the 1992 solution. The 2015 solution is obtained from Michálek *et al.* (2018). The uplift contours (every 1 mm yr^{-1}) for Fennoscandia (NKG2016LU model, Vestøl *et al.* 2019) are shown as thin dashed lines. The location of shear zones and other structures are obtained from Olesen *et al.* (2002). BL, Bivrost Lineament; NSZ, Nesna Shear zone; SSZ, Sagfjord shear zone.

and 68°N) (Fig. 1) was deposited as a result of this process. The older part of the Naust formation was deposited *ca.* 2.8–1.5 Ma, and the youngest part was formed less than 200 000 yr ago (Rise *et al.* 2005). The total volume of the Naust formation is estimated to be 80 000 km^3, with a maximum thickness of over 1500 m (Evans *et al.* 2000).

2.2 Crustal structure of Nordland

In most parts of offshore Nordland, the crustal structure has been studied extensively using deep seismic surveys (e.g. Sellevoll 1983; Avedik *et al.* 1984; Mjelde *et al.* 1993; Breivik *et al.* 2017, 2020). In contrast, the crustal structure in the mainland area remains poorly constrained. But over the past decade, crustal models derived from receiver function and surface wave studies have been developed using temporary seismic networks (Ben-Mansour *et al.* 2018; Michálek *et al.* 2018; Mauerberger *et al.* 2020).

Earlier seismic studies (Avedik *et al.* 1984; Mjelde *et al.* 1993; Mjelde & Sellevoll 1993) suggested that the crust in southern Lofoten is thin (<30 km), based on the seismic profiles BNR and 1–88 crossing the Lofoten ridge (see Fig. 1 for locations of seismic profiles and station described here). Mjelde *et al.* (1993) interpreted that the crust becomes thinner towards the Lofoten ridge, where the Moho is as shallow as 20 km—as indicated by a strong seismic interface in profile 1–88. More recently, Mjelde *et al.* (2013) suggested that this seismic interface is not the Moho, but rather the top of an eclogitic body located in the lower crust. This led these authors to revise the Moho depth for the region, placing it below the eclogite layer at 25 km depth. Based on receiver functions, the crustal thickness beneath station LOF (see Fig. 1) was estimated at approximately 30 km (Ottemöller & Midzi 2003). Michálek *et al.* (2018) estimated that the crustal thickness beneath the southern Lofoten-Vesterålen is between 20 and 25 km. Based on profile S83, Sellevoll (1983) suggested a thin crust for Lofoten-Vesterålen (between 20 and 26 km) with the southern part being the thinnest. Further to the north, the crust in the northern Lofoten-Vesterålen is thicker—around 36 km—based on profile 6-03 (Breivik *et al.* 2017). Using a combination of seismic lines 8-03 and 6-03, Breivik *et al.* (2020) suggested that the crustal thickness for the whole Lofoten-Vesterålen is actually greater than what has been interpreted previously. This shows that despite years of investigations, the depth of the Moho below southern Lofoten is still debated.

Recent broad-band seismological studies provide more information on the onshore crustal structure. Crustal thickness derived using receiver functions from stations deployed in northern Norway and Sweden (Fig. 1) showed a gradual change of crustal thickness from 38 km along the Caledonides to 43 km in the Baltic shield (Ben-Mansour *et al.* 2018). This gradual change does not reflect the topography variation at the surface. Therefore, Ben-Mansour *et al.* (2018) suggested that the surface topography cannot be explained by the classical isostatic model.

In addition to seismological experiments, potential field including gravity and magnetic methods have been used extensively to study the crustal structure in Nordland (e.g. Olesen *et al.* 2002; Tsikalas *et al.* 2005; Maystrenko *et al.* 2017). These methods provide constraints where seismic data is absent, especially in the mainland area. Maystrenko *et al.* (2017) performed 3-D density modelling to investigate the lithosperic structure along the Lofoten-Vesterålen margin. They constrained their model with various sources of crustal thickness observations: Ben-Mansour *et al.* (2018) for the mainland, Breivik *et al.* (2017) for the northern Lofoten-Vesterålen where the Moho is as deep as 36 km, and Mjelde *et al.* (1993) for the southern Lofoten-Vesterålen where it was suggested that the Moho depth is 22 km. The crustal thickness compiled by Maystrenko *et al.* (2017) is shown in Fig. 1. However, recently Breivik *et al.* (2020) pointed out that the crustal thickness used by Maystrenko *et al.* (2017) for the southern Lofoten-Vesterålen islands should be greater and questioned the existence of a lower density mantle. We will shed some additional light onto this question with the results from our tomography.

The gravity data point to two distinct anomalous features: Lofoten has a high gravity anomaly, whereas a large part of the mainland has a low gravity anomaly (Olesen *et al.* 2010). Gradmann *et al.* (2017) argues that the elevated Lofoten ridge is not isostatically supported if the Moho is shallow, but that a crustal root (e.g. eclogitic layer) is needed. In addition, low-density mantle rocks can play a role (Maystrenko *et al.* 2017). The mainland low gravity anomaly is possibly associated with low density rocks within the crust or the upper mantle (Gradmann & Ebbing 2015; Maystrenko *et al.* 2017). The location of the low gravity anomaly coincides with the northwest extension of the Transscandinavian igneous belt. However, other igneous belt locations in Scandinavia are only associated with minor gravity lows (Gradmann & Ebbing 2015).

2.3 Intraplate seismicity and present-day stress

Nordland has the highest seismicity rate in mainland Norway, with earthquakes occurring mostly along the coastal area and offshore along the shelf edge (Fig. 2). The 31 August 1819, M 5.9 Lurøy earthquake, the largest known earthquake in mainland Norway, was widely felt in Scandinavia and triggered major rockfalls and landslides in the epicentral area (Måntyniemi *et al.* 2020). In recent times, a number of earthquake swarms have occurred mainly along the coast, for example 1978–1979 Meløy (Bungum *et al.* 1979, 1982), 1992 Steigen (Atakan *et al.* 1994) and Jektvik (April 2015–March 2016, Janutyte *et al.* 2017a; Michálek *et al.* 2018). Previous studies suggested that the Meløy and Jektvik swarms had normal and oblique-normal focal mechanisms with approximately coast-perpendicular extensional direction (Bungum *et al.* 1979; Janutyte *et al.* 2017a; Michálek *et al.* 2018). Further to the north, the 1994 Steigen swarm occurred near the Sagfjord shear zone. The composite focal mechanism for the Steigen swarm is oblique-normal (Atakan *et al.* 1994).

In the offshore area, the earthquakes are generally thought to be associated with thrust faulting (Bungum *et al.* 1991; Hicks *et al.* 2000b). However, the focal mechanisms are mostly derived from mainland stations and are poorly constrained. As a result, it is not unexpected that the focal mechanisms vary quite significantly (Fig. 2). Since the earthquakes are generally smaller than magnitude 5, only one event (M_w 5.1 on 4 August 2003) with thrust mechanism has been reported in the global CMT catalogue (Ekström *et al.* 2012, Fig. 2).

Present day stress in Nordland is influenced by several regional and local sources (Bungum *et al.* 2010). At the regional scale, Nordland experiences compressive ridge push stress from the Mohns ridge (Fig. 1). Scandinavia is also influenced by glacial isotatic adjustment (GIA) with the Gulf of Bothnia being the area with the highest uplift (9–10 mm yr^{-1}, Steffen & Kaufmann 2005; Keiding *et al.* 2015; Vestøl *et al.* 2019, Fig. 1). Keiding *et al.* (2015) showed that the coast of Nordland has the highest uplift gradient even though this region has a comparatively low uplift rate (3–4 mm yr^{-1}). To give a clear picture of the uplift in Nordland and in Fennoscandia, we plotted the NKG2016LU land uplift model, developed using geodetic observations and GIA model (Vestøl *et al.* 2019) in Fig. 2.

The effect of GIA can create extension around the edge of the ice load which in Nordland lies approximately around the coastal area (Wu & Hasegawa 1996; Fjeldskaar *et al.* 2000). The models of Fjeldskaar *et al.* (2000) suggest compression beyond the ice edge, consistent with the present-day stress regime offshore Nordland. Rapid sedimentary loading offshore and topography effects can also influence the stress regime in the area to some extent. The combination of these local effects, tectonic stress and lateral variations in the lithosphere seems to control the stress state in the region (e.g. Fejerskov & Lindholm 2000; Bungum *et al.* 2010; Keiding *et al.* 2015; Gradmann *et al.* 2018).

3 DATA AND PREPROCESSING

To develop a high resolution seismic velocity model, we conducted 3-D seismic traveltime tomography. We used *P*- and *S*-wave arrival times from earthquakes and mining blasts recorded in Nordland and the surrounding region. Furthermore, to obtain information on earthquake mechanisms, we used first motion polarities and amplitude ratios of selected earthquakes. We recomputed the focal mechanism catalogue published by Michálek *et al.* (2018), who used a 1-D velocity model to derive the solutions. Here we tested the use of a 3-D velocity model to improve focal mechanism estimation and get better information on the crustal stress.

Most arrival time data used in this study were obtained from the Norwegian National Seismic Network (NNSN) catalogue for the period of 2007–2019 (Ottemöller et al. 2018), which contains data from permanent NNSN (Ottemöller *et al.* 2021) and Norsar (Schweitzer *et al.* 2021) stations and from the temporary Neonor2 deployment (2013–2016, Michálek *et al.* 2018). We manually picked arrival times from additional temporary and permanent networks deployed in the region, that is the Swedish National Seismic Network (SNSN, 2013–2016, Lund *et al.* 2021), Finnish National Seismic Network (FNSN, Veikkolainen *et al.* 2021), Scanlips2 (2007–2009), Scanlips3D (2013–2014, England *et al.* 2016) and Scanarray (2013–2016, Thybo *et al.* 2021). In total, these manual picks contribute approximately 20 per cent of the phase picks in the new combined data set used in this study. The ray paths from the NNSN catalogue are dominated by coast-parallel azimuths (Fig. S1), but the additional phase picks have increased the ray coverage mostly in coast-perpendicular azimuths (Fig. S1). The data set contains the 2015–2016 Jektvik swarm and a small cluster of events in Steigen that occurred in 2008–2009 (Fig. 2). The cluster in Steigen is located in the vicinity of the 1994 Steigen swarm. In addition to earthquake data, we also included a few mining related events to improve the coverage. The events occurred in the Kvannevann mine in the southern part of Nordland and are labelled as mining events in the NNSN catalogue.

All phase picking was done using the Seisan software package (Havskov & Ottemoller 1999; Havskov *et al.* 2020). We assigned three levels of phase pick quality: (1) clear impulsive, (2) clear emergent and (3) unclear emergent, and assigned a corresponding weight in the hypocentre determination, that is 100, 75 and 50 per cent, respectively. Other phase picks with lower quality were discarded, and observations at stations with timing issues were removed. A systematic estimate of the picking errors is not available as we used picks from different sources. We made some visual estimation of the errors, and decided to use a slightly conservative error estimate of 0.1 s.

We tuned the data set by first locating all events with a 1-D velocity model, and then systematically selecting only high quality events and reliable stations for further use in the tomography. We removed stations that had fewer than 15 observations which may indicate low data quality at the stations and to avoid the artefacts in the velocity model near the stations. The events were located using the Hypocentre program (Lienert & Havskov 1995) and the traveltimes computed with the 1-D NNSN velocity model (Havskov & Bungum 1987). Then we selected earthquakes based on the following criteria: (1) local magnitude $M_L \geq 0.5$, (2) recorded by a minimum of eight stations and (3) azimuthal gap $\leq 200^\circ$. To avoid the ray paths being dominated by events from the same area, we used a larger magnitude criterion ($M_L \geq 1.0$) for the area of the Jektvik swarm, which resulted in 150 events. Out-of-network offshore earthquakes have a larger azimuthal gap and larger location uncertainties. However, these events can improve ray coverage at depth and near the edge of the model (Koulakov 2009). In our case, the out-of-network events improve ray coverage in the offshore region. For these events, we required a depth of less than 25 km and a minimum number of 15 recording stations.

The final data set consists of 527 earthquakes with a total of 7868 *P*-wave and 6470 *S*-wave arrival times recorded by a total of 79 seismic stations for the period of 2007–2019. Approximately 85 per cent of our events have an azimuthal gap $\leq 180^\circ$ and the peak of the azimuthal gap distribution is $\sim 100^\circ$. In addition, we

used 16 mining events, which yield an additional 161 *P*-wave and 153 *S*-phase observations. Since the mine is relatively small, approximately 3 km^2, we did not locate these events but we fixed the hypocentres to the centre of the mine.

The data set needed for the focal mechanism calculation are the first motion polarities and the SH/P amplitude ratios. We recomputed solutions from (Michálek *et al.* 2018), which had been computed using the permanent NNSN and temporary Neonor2 networks. Here we added measurements from additional temporary stations, for example Scanlips3D and Scanarray. We computed the focal mechanisms for 41 events that have at least six clear first motion polarities. The SH/P amplitude ratios were computed using an automatic procedure integrated in Seisan (Michálek *et al.* 2018). We only used amplitudes of the direct phases, that is Pg and Sg phases and limited the epicentral distance to 100 km. The *P* and SH displacement amplitudes were measured in the frequency domain on the vertical and transverse components, respectively.

4 METHODS

In order to produce 3-D seismic V_P and V_P/V_S ratio models for the Nordland region, we applied a procedure comprising the following two steps: (1) 1-D V_P and V_S inversion used to find 1-D initial model for tomography and (2) 3-D V_P and V_P/V_S ratio inversion. The 3-D take-off angles computed in step (2) were later used to improve the focal mechanisms. In this section, we describe details of the methods that were applied.

4.1 Seismic velocity inversion

The seismic tomography results strongly depend on the starting model (Kissling *et al.* 1994). Consequently, as a first step, we inverted for a 1-D velocity model that will be used as starting model in the 3-D inversion. We used the Velest code (Ellsworth 1978; Kissling 1995), which performs velocity inversion simultaneously with hypocentres and station delays. The station delay terms are introduced to accommodate for near-surface and large scale velocity heterogeneity (Husen *et al.* 2011). Here we tested two input 1-D velocity models: (1) the 1-D NNSN velocity model from Havskov & Bungum (1987) and (2) the average Crust1.0 model for the entire study area (Laske *et al.* 2013). We found that the average crustal thickness in the area is ≈40 km from Crust1.0 and the Moho depth compiled by Maystrenko *et al.* (2017). We tested different crustal thicknesses of 35, 40 and 45 km for both input 1-D models. The layer thicknesses were not inverted, but were adjusted during the preparation. We divided the 1-D model into 5 km layers and used the velocities interpolated from the respective input model. A layer adjustment test was performed by inverting for velocities for the models, and then we combined the layers with similar velocities.

To test the range of feasible input models, we followed the procedure of Shiddiqi *et al.* (2019) by creating 500 model variations for each initial model. This was done by randomly perturbing the V_P and V_S for each layer within a range of ±10 per cent), but keeping the V_P/V_S ratio within the range of 1.6–1.9. We only accepted the results within the lowest 10 per cent root mean square (RMS) residuals, which were then averaged. The next step was to refine the averaged velocity models to obtain the final models and the respective station delays by performing an additional inversion on it. In this stage, we assigned a higher damping weight to the velocity model, so that the velocity model is not changed significantly during the inversion. The preferred minimum 1-D velocity model, which was selected based on its traveltime residuals, is presented and described in Section 5.1.

The next step was to perform the 3-D traveltime tomography using the SIMULR16 code (Bleibinhaus 2003; Bleibinhaus & Gebrande 2006; Bleibinhaus & Hilberg 2012), which is a modified version of the well-established SIMUL family codes (Thurber 1983; Evans *et al.* 1994; Thurber & Eberhart-Phillips 1999; Rietbrock 1996). The SIMULR16 code uses a damped iterative least-square inversion scheme to obtain 3-D V_P, V_P/V_S ratio, and station delays. To compute the traveltime, the code employs a combination of approximate ray tracing (ART) and pseudo-bending method (PB) to calculate the traveltimes. Bleibinhaus (2003) modified the ART and included an iterative segmentation for PB to compute more accurate ray paths at regional distance within a heterogeneous medium. These modifications improve the accuracy of the ART-PB ray tracer by more than 1 order of magnitude for distances above 140 km (Bleibinhaus 2003).

To produce a robust 3-D model, we performed a series of inversions where the complexity increases as the number of inversion grid nodes increases and the horizontal grid spacing decreases. First, we ran the inversion on a coarse grid model (6 × 8 × 12 grid nodes; smallest horizontal grid spacing: 100 km) using the preferred 1-D velocity model as the starting model (See Fig. S7 and Section 5.1). Then, we performed two additional inversions with refined grid spacing, a medium grid (9 × 13 × 12 grid nodes; smallest horizontal grid spacing: 50 km), and a fine grid (18 × 23 × 12 grid nodes; smallest horizontal grid spacing: 25 km; see Fig. S2). The final model in each inversion stage is used as the starting model for the next stage. We used ray density and the checkerboard test results to evaluate the model resolution throughout the process. The final 3-D model, which we present and describe in Section 5.2, is the result of the inversion using the fine grid nodes. The distributions of ray paths and fine grid nodes are shown in Fig. S2.

The observations were weighted based on the phase picking quality (we applied the same weighting scheme as for the hypocentre determination in Data section), and traveltime residuals. The earthquake hypocentres and origin times were updated iteratively before the velocity inversion in each iteration. The hypocentres were fixed for the mining events, but the origin times were recomputed. We evaluated the reliability of earthquake depth at each inversion stage, especially for 'out-of-network' events. The inversions were repeated after we removed events that have unreliable locations. The damping parameters, which control the model perturbation in each iteration, are determined using a trade-off curve between model variance and data misfit.

4.2 Focal mechanism

Focal mechanisms provide important information about the stress regime of an active tectonic region. In order to obtain accurate focal mechanisms for selected earthquakes in Nordland, we used a combination of first motion polarities and SH/P amplitude ratios. Initially, we computed focal mechanisms by using the Focmec program (Snoke 2003) based on a 1-D model, but then transitioned to our resulting 3-D model to allow for improved take-off angles. Previous studies have demonstrated that the use of 3-D velocity models can improve the focal mechanism solutions (e.g. Takemura 2016; Newrkla 2019). We used the final hypocentres, determined using the 3-D seismic velocity model, for both analyses. Focmec performs a grid search over strike, dip and rake and finds solutions that are within given error criteria. We computed the take-off angles,

emergence angles and azimuths using ray paths obtained from the SIMULR16 code.

Amplitude ratios are useful to constrain the solutions that were initially obtained using polarities only. The amplitude ratios between *P* and *S* waves were corrected for attenuation and free surface and then depend only on the radiation pattern (e.g. Havskov & Ottemöller 2010). The free surface correction requires V_P/V_S ratio (here a constant value of 1.74 is used) and the emergence angles. The attenuation correction is based on the quality factors *Q* for *P* and *S* waves. Since we only have information for Q_{Lg} for mainland Norway, we assume that Q_P and Q_S have the same value as $Q_{\rm Lg}$ and we adopted $Q_{\rm Lg} = 529f^{0.42}$ (Demuth *et al.* 2019). To assess the quality of amplitude ratios, we used the amplitude ratio misfit, which is the difference between the observed and synthetic SH/P amplitude ratios. To ensure the solution's quality, the amplitude ratios that have logarithmic misfits larger than 0.2 were rejected (see the Focmec manual (Snoke 2003)).

We computed the focal mechanisms following a two-step approach described in Halpaap *et al.* (2019). First, the solutions were determined using polarities alone. We proceeded to the second step if the solutions were similar (i.e. *P*- and *T*-axes fall into small area on the lower hemisphere projection). Then we refined the solutions by combining polarities and SH/P amplitude ratios computed in the frequency domain. We did not allow for any polarity error, and the maximum number of rejected amplitude ratios had to be less than 50 per cent of the observations. The poorly constrained events were removed—that is those with more than 50 solutions for a grid spacing of 2°. We used the solution uncertainties to evaluate the solution qualities similar to Hardebeck & Shearer (2002), but here we adopted more relaxed criteria. We considered the absolute maximum difference in strike, dip and rake as an indicator of solution uncertainties and assigned three solution qualities: (1) events that have all solution uncertainties less than 25° were given quality A, (2) events that have solution uncertainties (in either strike, dip or rake) larger than 25° and less than 45° were given quality B and (3) events that have larger uncertainties or events that have more than 50 solutions were given quality C. We only considered events with quality A and B as stable solutions that can be used for further analysis.

5 RESOLUTION

5.1 Hypocentre error estimation

In each stage of the velocity inversion, the hypocentres are relocated and their quality strongly affects the velocity model. In the SIMULR16 code, the location error is estimated using the variance and the outer product of an SVD-derived general inverse operator (see Klein 2002; Halpaap *et al.* 2018). The variance itself is a combination of the picking error, and weighted traveltime residuals. We assigned a conservative value of 0.1 s for the picking error (see Section 3). Fig. 3(a) shows that the RMS of traveltime residuals are reduced by about 20 per cent and the average location errors are reduced by about 30 per cent during the three stages of tomography inversion. The station delays are reset to zero at the beginning of each stage. Therefore, the starting RMS in medium and fine grids are higher than the previous iteration of the larger grids. Furthermore, we also evaluated the solutions convergence by showing the velocity and hypocentre changes for each iteration in Figs 3(b) and (c). In each stage, largest solution changes happened in the first few iterations, and then the solutions did not change significantly afterwards. This pattern is expected and indicates that the solutions converge.

5.2 Tomography resolution tests

To evaluate the resolution and robustness of our tomography results, we conducted a series of synthetic tests. We performed the tests to investigate how well synthetic anomalies can be recovered, in terms of their size, location and strength, by our inversion set-up. First, we created two types of synthetic velocity models: (1) checkerboard velocity models and (2) synthetic models based on velocity anomalies in the tomography results. Then we calculated synthetic traveltimes using the final hypocentres and the synthetic velocity models. We added random Gaussian noise to the traveltimes with a standard deviation of 0.1 second based on our picking error estimate. We did not directly shift the hypocentres, but the starting locations are shifted during the initial adjustment before the velocity inversion due to the noise and the use of an initial velocity model. We then inverted the synthetic data to obtain V_P, V_P/V_S ratio along with the hypocentres.

In a first series of resolution experiments, we performed checkerboard tests by alternately perturbing the final 3-D velocity model by ±5 per cent. The checkerboard test results for three depth slices (8, 24, 32 km) and coast parallel cross-sections are shown in Fig. 4. The tests show that V_P and V_P/V_S ratio can be recovered (Fig. 4) and we are able to recover the central part of the model (Lofoten–Vestfjorden basin–coastal area–and some part of the mainland area) down to the Moho depth. In this central part, at shallow depth, both shape and anomaly strength are quite well resolved and in the deeper part, we can still recover the anomalies but they are weaker and start to smear. In the northeastern corner of the model, we can recover the checkerboard anomalies but smearing affects the results. The anomalies are getting weaker in the mid-crust (17–24 km) due to limited number of direct ray paths crossing this part of the model. This area is dominated by refracted ray paths (Pn and Sn phases), and has a limited number of direct ray paths (Pg and Sg). This ray path distribution can resolve the Moho well, but not the shallower structure in the corners of the model.

In a second series of resolution tests, we performed synthetic anomaly recovery to evaluate whether prominent velocity anomalies expected in our tomographic models are more likely to be real features or artefacts of the inversion. We performed two such synthetic anomaly recovery tests as described in the following:

(i) Moho step

Earlier results (e.g. Maystrenko *et al.* 2017; Michálek *et al.* 2018) showed that there is a transition between the shallow Moho in the southern Lofoten and deeper Moho in the mainland. Our early tomography tests indicated the existence of a sharp transition, which we refer to as Moho step. Here we tested the robustness of this Moho step. We created a synthetic 3-D V_P model with a simplified Moho step. This was achieved by using the initial 1-D model with Moho depth of 40 km onshore, and by adapting a shallow Moho model of 27 km for southern Lofoten. Then we inverted the synthetic data by following our inversion grid scheme: starting from coarse grid, then medium and fine grid size model. The synthetic model and inversion results are shown in Fig. S3. We were able to recover the shallow Moho and the Moho step beneath southern Lofoten in profiles B–B' until E–E' (see Fig. 4 for the location of the profiles). The Moho transition in profile F–F' appears to be smoother due to limited ray path coverage.

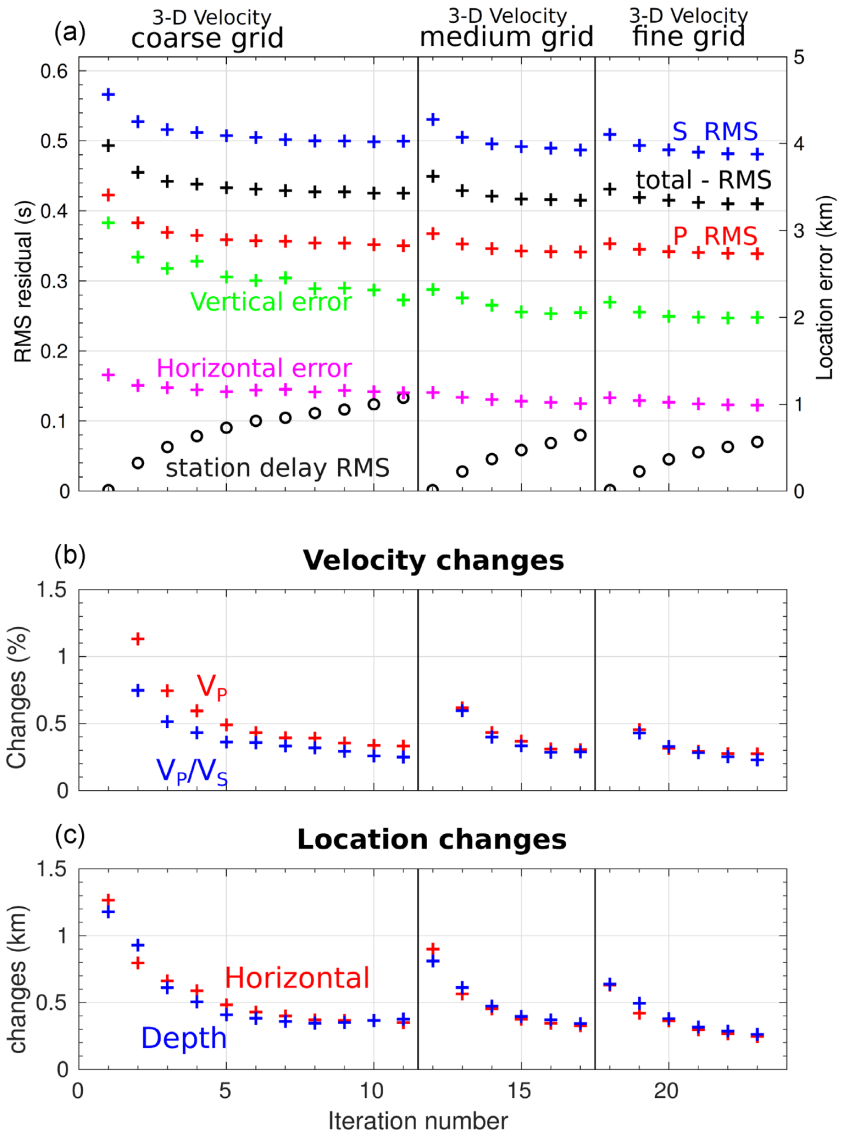

Figure 3. (a) Plot of traveltime RMS residuals, station delays RMS, and the average location error changes for each iteration. At the beginning of each inversion stage, the station delays are set to zero. Therefore, the starting RMS in medium and fine grids are higher than the last iteration of the larger grids. (b) Plot showing the average velocity changes. The change is the difference between the current iteration (n) and the previous iteration (n–1) for each grid. (c) The average location changes for each iteration.

Next we verified whether the Moho step can be artificially created by our inversion set-up. Previous models showed that the Moho transition from southern Lofoten towards the mainland is smooth (e.g. Maystrenko *et al.* 2017). Therefore, we created an additional synthetic test by modifying the simplified Moho step model. As opposed to an abrupt change in the Moho depth, we modified the model to make the transition smoother. Then we inverted the synthetic data using the same inversion scheme. The initial model and inversion result are shown in Fig. S4. The inversion results show that the Moho transition is relatively smooth. These tests showed that we can resolve the shallow Moho beneath southern Lofoten and the Moho step feature, and that the Moho step is unlikely to be an artefact.

(ii) Robustness of the anomalies near the Moho step

Uneven ray path distribution is usually expected in earthquake traveltime tomography. Velocity anomalies can influence the ray path distribution as well, by focusing or defocusing the ray path. In our case, seismic events are concentrated along the coast near the Moho step. Therefore, the ray paths become concentrated in this area (see cross-section plots of the ray paths in Fig. S5) and it is important to verify that a high V_P/V_S ratio anomaly is not an artefact due to uneven ray path distribution.

To achieve this aim, we performed a set of synthetic tests by creating three synthetic models: (1) model with constant V_P/V_S ratio but added higher random Gaussian noise with a standard deviation of 0.2 s, (2) model with low V_P/V_S ratio anomaly in the offshore region and (3) model with high V_P/V_S ratio anomaly in the onshore region. In all of these models, we do not introduce any anomalies near the step. The synthetic models and the results are shown in Fig. S6.

From these tests, no strong velocity anomaly is introduced near the Moho step. Although there are small patches of high V_P/V_S ratio perturbation near the step, the anomaly strength is less than 1 per cent. This could be caused by the random noise added to the

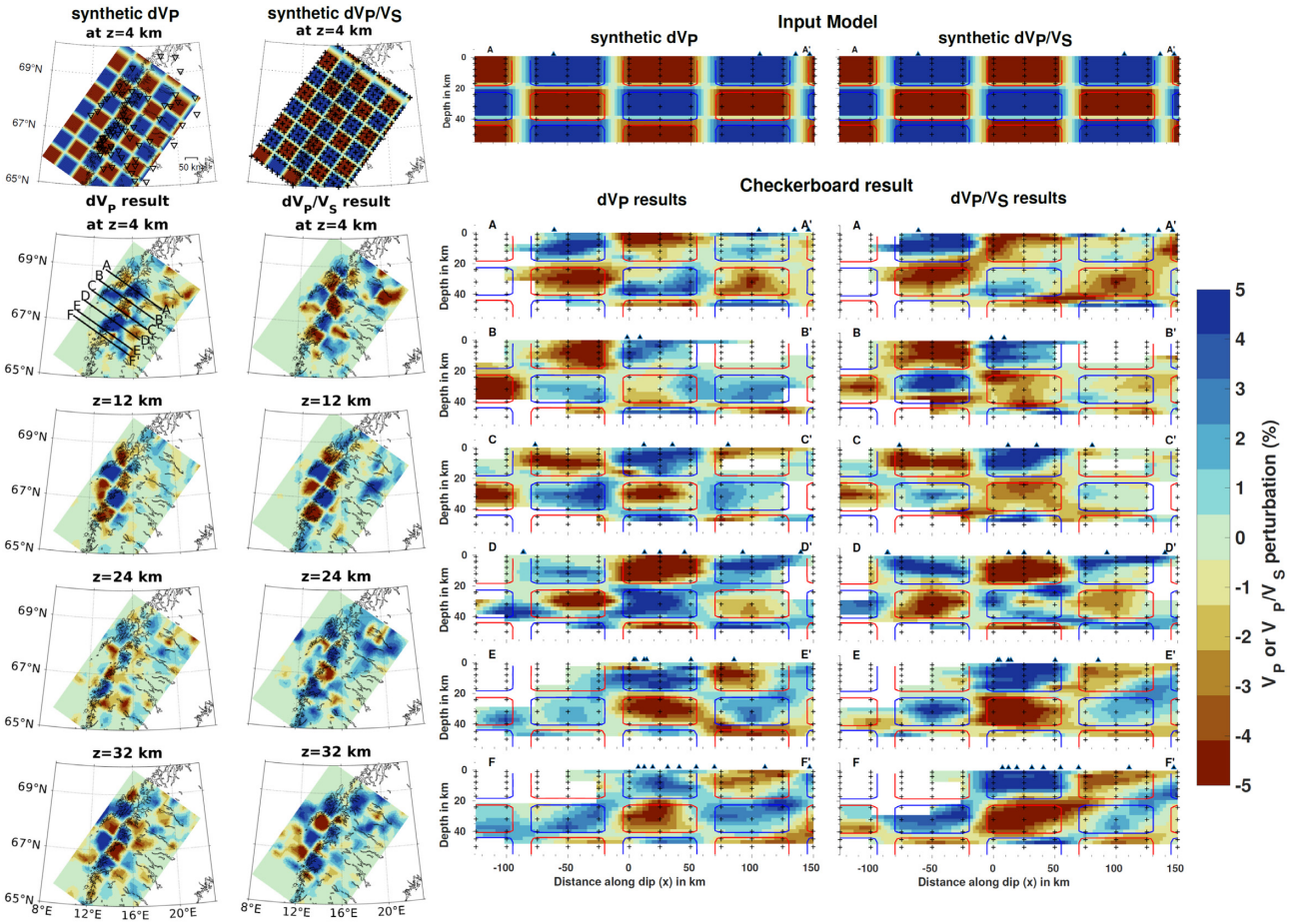

Figure 4. Checkerboard test for V_P and V_P/V_S ratio in the map view slices and cross-sections. The input synthetic model, created by alternately perturbing the final 3-D velocity model, is shown in the top row. All velocity plots are shown as the perturbation to the final 3-D velocity model. Stations (open inverted triangles) and inversion grid positions (crosses) are shown on the map view of synthetic V_P and V_P/V_S ratio models, respectively. The cross-section lines are shown on the map view V_P inversion result at 4 km depth. In the cross-section plots, grid node positions are also shown as cross symbols. The red and blue boxes highlight the area with low and high perturbation inputs, respectively.

synthetic data. Therefore, we conclude that the Moho step feature does not create an artificial anomaly.

6 RESULTS

6.1 1-D velocity inversion

We tested six input models which consider several Moho depths, that is 35, 40 and 45 km and the output models are shown in Fig. S7. The NNSN-based models contain four crustal layers and the Crust1.0-based models consist of six layers. All 1-D velocity models have quite similar velocities for depth down to 20 km, and the largest variation occurs in the lower crustal and the mantle velocities. We found that the inversion using the averaged Crust1.0 velocities with the Moho at 40 km as starting model gives the lowest overall RMS residual. The preferred 1-D V_P, V_S and V_P/V_S ratio are shown in Fig. 5. All accepted inversion results tend to converge to a small range of parameter values except for V_P in the lower crust, between 20 and 40 km depth, where the results are quite spread out, especially for V_P. This pattern likely indicates strong lateral variation of V_P due to strong differences in crustal thickness, which cannot be captured by a 1-D velocity model. V_S is not as spread out as V_P because of the *S*-ray paths sampled a smaller area of the lower crust due to a smaller number of *S*-picks for stations further inland.

The *P*- and *S*-wave station delays for the preferred velocity model are shown in Figs 5(b) and (c). We chose permanent station MOR8 as the reference station, because it is located near the centre of the model, and was in operation throughout the period of our event catalogue. The positive and negative station delays represent late and early arrival times, respectively (e.g. Wright 2008; Midzi *et al.* 2010). Comparison of the *P*-wave delays for all velocity models are shown in Fig. S8. The contrast between delays on southern Lofoten and the mainland can be attributed to the deviation of the layer geometry, for example due to the crustal thickness variation. The stations on Lofoten have large negative *P*- and *S*-wave delays indicating large positive velocity perturbation along the ray paths beneath the southern Lofoten indicating a thinner crust. Stations on the mainland have positive *P*-wave delays, which correspond to negative velocity perturbation pointing towards a thicker crust.

6.2 Final hypocentre locations and 3-D velocity model

The hypocentre locations of 527 earthquakes used in the 3-D seismic tomography are shown in Fig. 6. There are only eight offshore events near the shelf edge that have reliable hypocentre locations. The

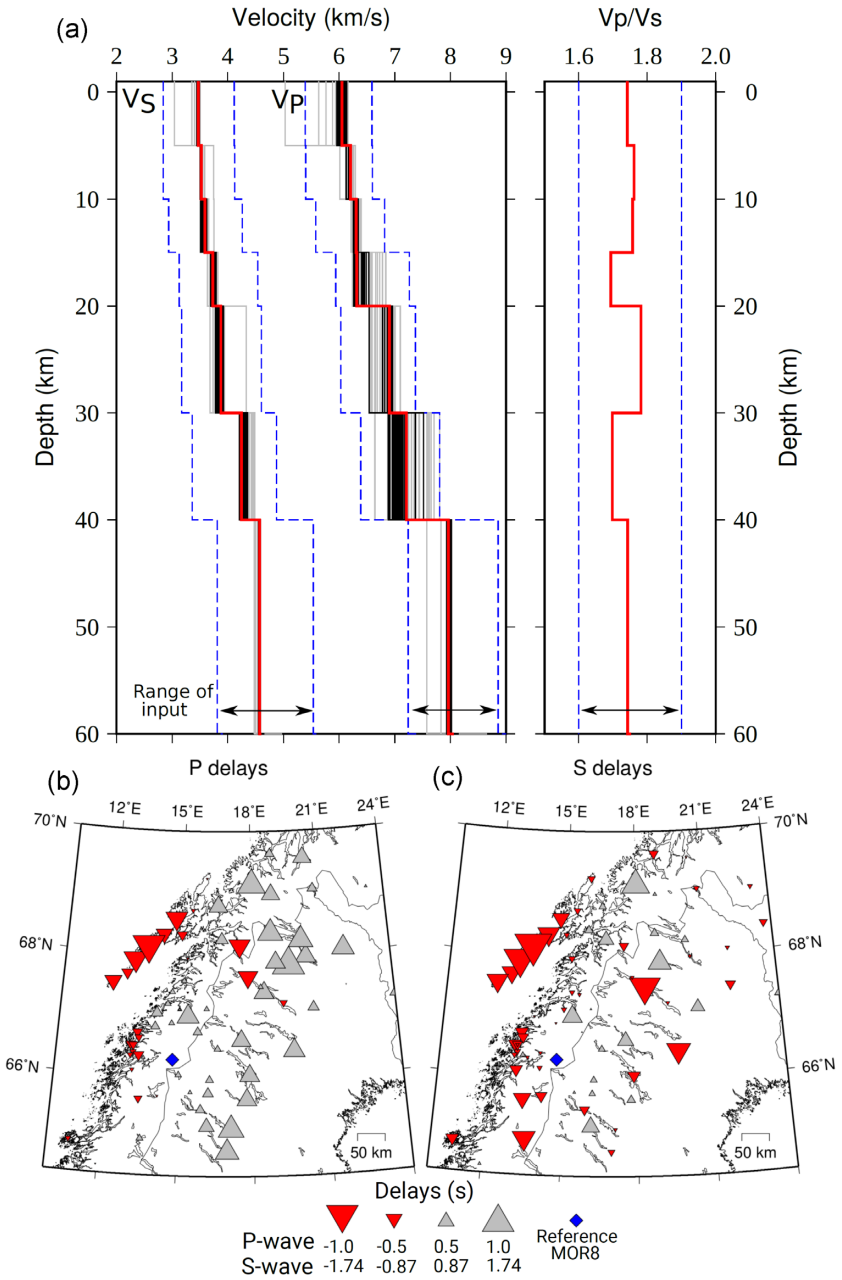

Figure 5. (a) Preferred 1-D velocity model. The final V_P, V_S and V_P/V_S ratio models are depicted by red lines. The range of input are shown as blue dashed lines. The inversion results are shown as grey lines and the accepted models are shown as black lines. Station delays for *P* and *S* waves are shown in (b) and (c), respectively. Symbols for *S*-wave delays are scaled down to the average V_P/V_S ratio, 1.74.

coastal seismicity is distributed from less than 5 km down to 18 km. The location of the Jektvik and Steigen swarms are highlighted in Fig. 6. In addition, we show the hypocentre distribution in the Jektvik and Steigen areas located using the four velocity models developed in this study: 1-D, 3-D coarse, 3-D medium and 3-D fine models in Figs S9 and S10.

The 3-D seismic tomography results are presented as coast-normal cross-sections in Fig. 7. The coast parallel cross-sections are also presented in Fig. S11. The depth slice of V_P and V_P/V_S ratio for depths 4, 8 and 12 km are shown in Fig. 8 and for for depths of 17, 32 and 40 km are presented in Fig. S12. Based on these results, we can estimate the position of the 'tomography Moho', indicated by a sharp gradient from 7.0 to 8.0 km s^{-1} (e.g. Husen *et al.* 2003). A number of tomography studies that used a similar approach to estimate the Moho depth adopted V_P contours between 7.25 and 7.4 km s^{-1}—see, for example studies of Diehl *et al.* (2009), Koulakov *et al.* (2015) and Leónios *et al.* (2021) which looked at Moho depths in the Alps, Himalaya and the Ecuadorian margin, respectively. Lange *et al.* (2018) used a higher V_P of 7.8 km s^{-1} as a proxy for the Moho in the Central Sumatra subduction zone. Here, we chose the V_P 7.6 km s^{-1} contour as an indicator of the continental Moho (Fig. 7) as this is close to the Moho depth derived from the receiver function studies for mainland Nordland from Ben-Mansour *et al.* (2018) and Michálek *et al.* (2018).

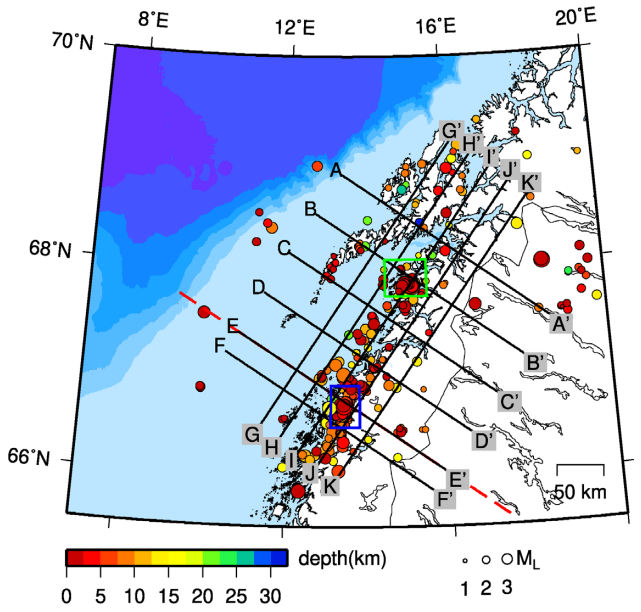

Figure 6. Distribution of final hypocentre locations. Large open circles mark the area of two earthquake swarms discussed in the text: Steigen swarm (green rectangle) and Jektvik cluster (blue rectangle). Positions of cross-section lines, shown in Figs 7 and S11, are depicted by black lines. Red dashed line is the location of extended E–E' section shown in Fig. 11. See Fig. 2 for the bathymetry scale.

We identified seven important features in our tomography results that are marked in Figs 7 and 8 with Roman numerals I–VII based on the order of their appearance in Section 7:

(i) A significant change of crustal thickness over a short distance (∼25 km) or Moho step exists beneath the Vestfjorden basin (in Sections B–B' to F–F'). In the northern part of Lofoten and Vesterålen, the crust is relatively thick (>35 km) and the transition towards the mainland (see Section A–A') is smoother. South of Lofoten (southern part of Lofoten islands and Lofoten ridge), the crust is thinner (around 27 km), and the Moho step is observed. The position of the Moho step comes closer to the coast as we move to the south. The crustal thickness in the mainland is greater than 40 km.

(ii) A thin layer of high V_P/V_S ratio anomaly (up to ≈1.84) exists at the upper crustal in the vicinity of the Steigen swarm within the Sagfjord shear zone (in Section B–B'). Below this anomaly, the V_P/V_S ratio is relatively low (down to ≈1.68).

(iii) A low V_P anomaly within the uppermost layer (Sections D–D' and E–E') extends from the mainland towards the Vestfjorden basin.

(iv) A low V_P/V_S ratio (down to ≈1.65) anomaly is observed at upper crustal depth (Sections E–E' and F–F') between 0 and 15 km depth. The low V_P/V_S ratio coincides with the Jektvik swarm.

(v) A high V_P/V_S ratio anomaly (up to ≈1.81) is observed around the Vestfjorden basin.

(vi) A high V_P/V_S ratio (up to ≈1.83) anomaly exists at upper-middle crustal depths further east in the model towards the area with high elevation (Sections E and F). The anomaly is observed between 5 and 15 km depth.

(vii) A high V_P/V_S ratio anomaly (up to ≈1.85) is observed at middle and lower crustal depths. The anomaly is most prominent in Sections C–C' and E–E'.

The interpretation of these features is presented in Section 7.

6.3 Focal mechanisms

We computed focal mechanisms for 41 events that have a minimum of six polarity observations. On average, each event has eight polarities. Based on our result, the focal mechanisms computed using the 3-D velocity model have smaller amplitude ratio misfits (average logarithmic misfits: 0.18) than the focal mechanism derived using 1-D velocity model (average logarithmic misfits: 0.43). We use solution range as an indicator of solution uncertainties. The 1-D velocity solution ranges are: strike 19°, dip 23° and rake 24° and the 3-D model solution ranges are reduced to: strike 10°, dip 7° and rake 16°. Fig. S13 demonstrates the improvement of focal mechanism solutions using the 3-D velocity model. This comparison also shows that the station positions on the focal sphere can vary significantly depending on the velocity model. Since we used the same hypocentre locations, the differences in take-off angles between 1-D and 3-D models are mainly caused by the variation of V_P, which can change the ray direction from downgoing to upgoing or the other way around.

Out of 41 events, we obtained reliable solutions for 21 events, that is 16 events of quality A and 5 events of quality B (Fig. 9). The remaining 20 events are categorized as quality C, and are not used in further interpretation. Most of the reliable solutions are normal and oblique-normal faulting mechanisms. The majority of events are part of the Jektvik swarm that have a near vertical *P*-axis and coast perpendicular *T*-axis (Fig. 9).

7 DISCUSSION

In following subsections, we discuss the interpretation of our velocity models and focal mechanism solutions, and their possible relation with the intraplate seismicity in Nordland.

7.1 Crustal thickness variation

From the 3-D V_P model, we estimated the crustal thickness, that here is defined as the thickness of crystalline crust plus overlying sediments. The differences between crustal structure of the southern and northern Lofoten-Vesterålen as well as the mainland area are already indicated by the *P*-wave station delays obtained from the 1-D velocity inversion, which reflect the deviation from the 1-D Moho depth of 40 km. The large negative delays in the southern Lofoten indicate the existence of a high velocity anomaly there, which possibly corresponds to a shallow Moho. The large positive delays in the mainland possibly correspond to thicker crust. Indeed, our 3-D V_P model shows variation from a thinner crust offshore towards a much thicker crust inland (Fig. 10). Along the Lofoten-Vesterålen islands (approximately SW–NE), the crustal thickness varies as well. The northern Lofoten-Vesterålen has crustal thickness around 35 km and further to the south the crust is thinner ∼27 km.

In mainland Nordland, our Moho depth estimates range from 40 to 47 km. This result is comparable to crustal thickness models derived by receiver function studies (Ben-Mansour *et al.* 2018; Michálek *et al.* 2018). A slight Moho depth variation is found along the coast where the crust further south is thinner (∼40 km, Section D–D' and E–E' in Fig. 7), and the crust beneath Steigen is thicker ∼47 km (Section B–B' and C–C' in Fig. 7). Further to the north, the crustal thickness is ∼42 km (profile A–A' in Fig. 7). This transition can be also seen in coast-parallel profile I–I' in Fig. S11.

Feature I in Fig. 7 shows an abrupt change in crustal thickness beneath the Vestfjorden basin, between southern Lofoten-Vesterålen and the mainland, which we refer to as a Moho step. With the

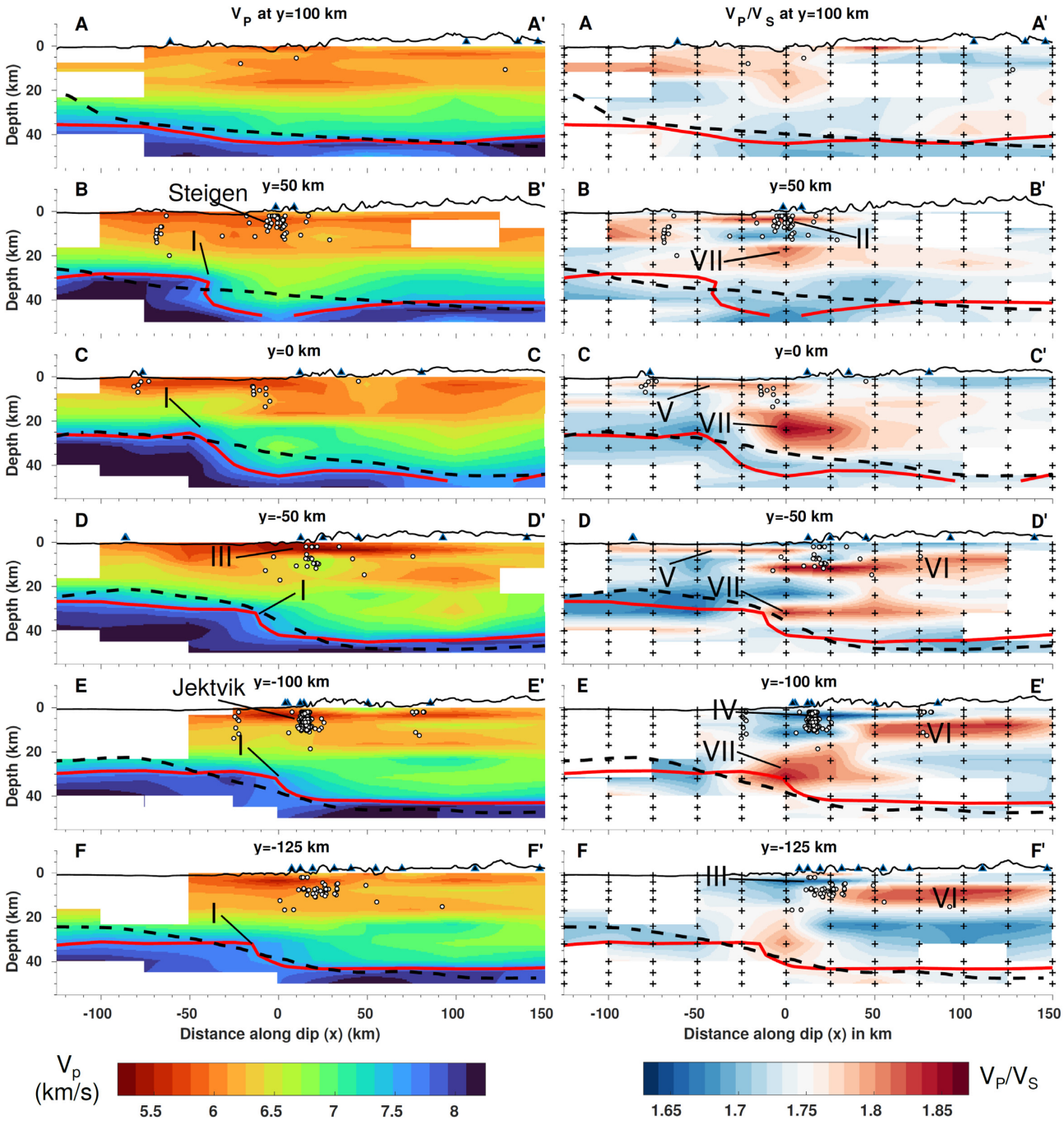

Figure 7. Coast normal cross-sections of V_P and V_P/V_S ratio across the resulting tomography model. Roman numeral labels are the features discussed in the text. Red lines are the contour of the 'Moho velocity' (V_P 7.6 km s^{-1}), and the dashed black lines is the Moho model compiled by Maystrenko *et al.* (2017). Hypocentres and stations are represented by white circles and black triangles, respectively. Surface topography (with 4× vertical exaggeration) is plotted on the top of each cross-section. The inversion grids are plotted in V_P/V_S ratio sections. See Fig. S2 for the coordinate system of the model.

resolution test in Section 5.2, we showed that the velocity inversion can recover such sharp Moho change. The sharp details of this transition were not previously resolved and were not included in the compilation by Maystrenko *et al.* (2017) as it builds on lower resolution input than what is afforded by our new tomographic results.

The crustal thickness variation around the Lofoten-Vesterålen islands has been discussed in recent publications (e.g. Breivik *et al.* 2017, 2020; Maystrenko *et al.* 2020b). As mentioned in the background section, there is an ongoing debate as to whether the crust is thin or not in southern Lofoten and in this section we show our results can contribute to this debate. The seismic profile 1-88 (see Fig. 1) from Mjelde *et al.* (1993) has previously been used as the main constraint on crustal thickness in the southern Lofoten, particularly beneath the Lofoten Ridge. The model from Mjelde *et al.* (1993) suggested that the crustal thickness here is as low as 20 km in a narrow area below the Lofoten Ridge. In an updated interpretation, Mjelde *et al.* (2013) suggested that the crust is thicker than in their earlier model (≥25 km). Further to the south of profile 1-88, using the Blue Norma profile (BNR profile in Fig. 1) Avedik *et al.*

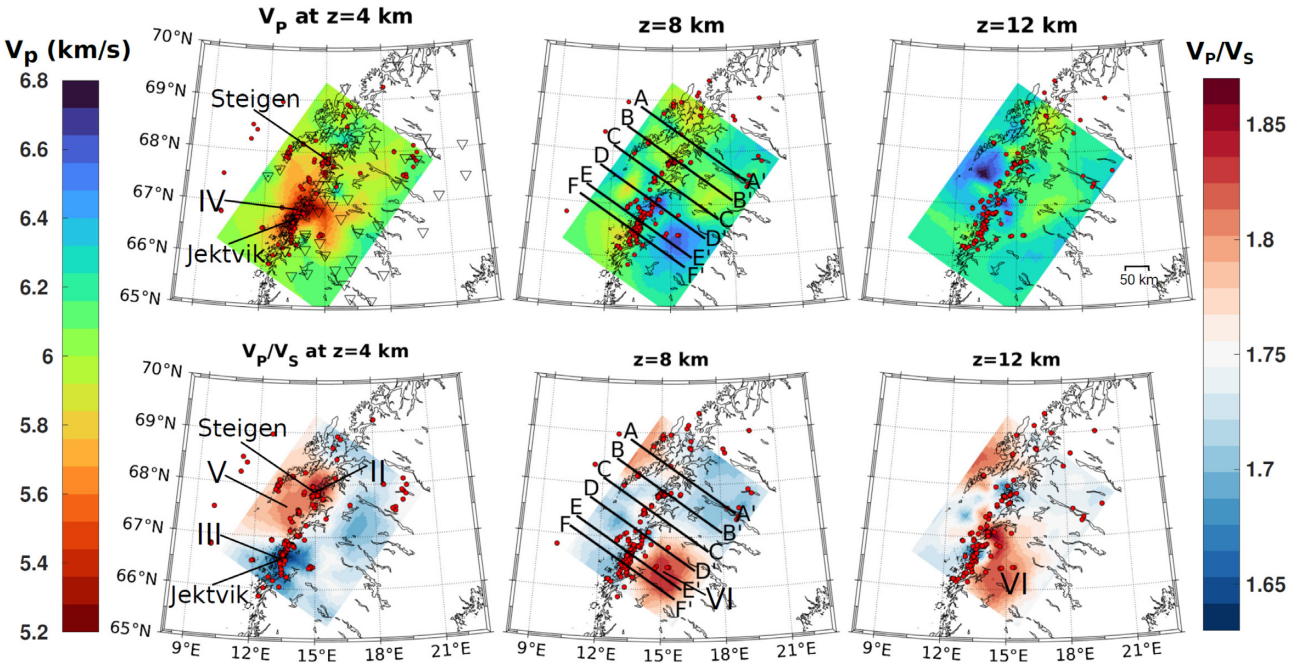

Figure 8. Horizontal depth slices of V_P and V_P/V_S ratio for the upper crustal depth. The colour scale for V_P is readjusted for a lower velocity range. Positions of the coast parallel cross-sections are shown at 8 km depth slices.

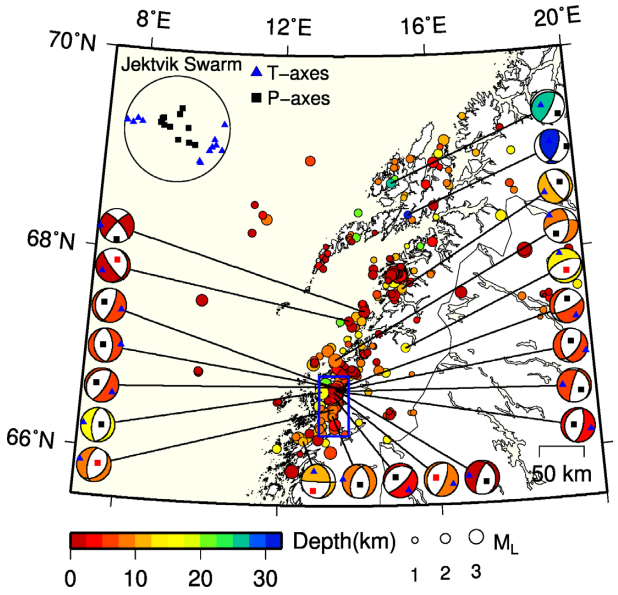

Figure 9. Distribution of the accepted focal mechanism solutions (Quality A and B). Small rectangles and triangles in the solutions represent the *P*- and *T*-axes, respectively. The quality A and B solutions are labelled with black and red triangles, respectively. The open blue rectangle is the location of Jektvik swarm. The *P*- and *T*-axes of solutions from Jektvik are shown in upper left circle.

(1984) also inferred that the region here has thin crust. In contrast, using profile 8-03 (Fig. 1), Breivik *et al.* (2020) proposed that the crust beneath southern Lofoten is thicker (> ∼30 km).

Our larger crustal thickness estimates in the northern Lofoten-Vesterålen are similar to those of Breivik *et al.* (2017), and the shallower Moho depth in the southern Lofoten-Vesterålen is comparable to that proposed by Mjelde *et al.* (2013). In Fig. 7, the profile A–A' represents the northern Lofoten-Vesterålen area with a thicker crust, and profiles B–B' until E–E' represent the area with a thinner crust in the southern Lofoten-Vesterålen. We suggest that the transition occurs between profiles A–A' and B–B' (also see profile G–G' in Fig. S11). Mjelde *et al.* (2013) proposed the existence of high velocity eclogitic layer in the lower crust of the Lofoten ridge. However, the proposed eclogite in the lower crust is not resolved in our model due to limited rays and our inversion grid spacing. Still we observe a thinner crust in the southern Lofoten-Vesterålen (∼27 km), and conclude that the model of thinner crust in the southern Lofoten-Vesterålen is valid.

7.2 Crustal Structure and composition

The main upper crustal velocity anomalies are located in the vicinity of two distinct seismicity clusters: the Steigen swarm in the north, and the Jektvik swarm in the south. In the vicinity of the Steigen swarm, we observe relatively low V_P and high V_P/V_S ratio at shallow depths, and low V_P/V_S ratio at greater depths (anomaly II in Figs 7 and 8). Whereas in Jektvik, very low V_P (anomaly III) and low V_P/V_S ratio are observed (anomaly IV). The V_P around Jektvik swarm is significantly lower and extends over a larger area, while the low V_P around Steigen is more localized.

The low V_P in both regions can be an indication of fractured rocks and fluids (e.g. Unsworth & Rondenay 2013). The effect of fracture and fluid content can also play an important role in the variation of V_P/V_S ratios at shallower depth (e.g. Wang & Ji 2009; Kuo-Chen *et al.* 2012). However, the V_P/V_S ratio sign depends on the pore pressure, aspect ratio of the pore, fluid content, and the Possion's ratio of the host rocks (Takei 2002; Brantut & David 2018). While

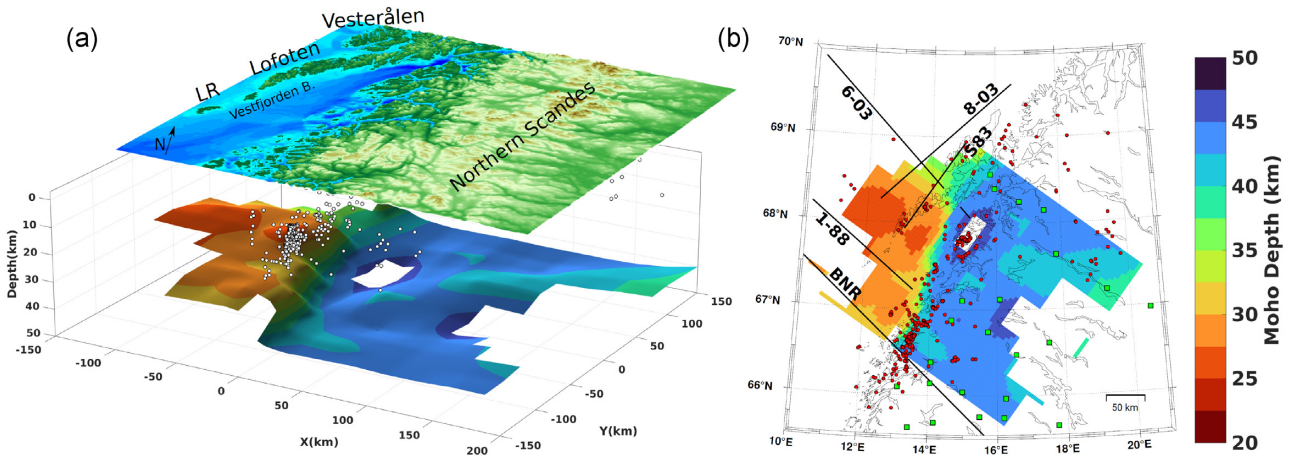

Figure 10. (a) 3-D block model of Moho surface extracted from the 3-D V_P model. Earthquake hypocentres are shown as white circles. The vertical axis has 2× exaggeration. (b) Map view of the Moho surface. Earthquake are shown as red circles. Black lines are the seismic lines discussed in the text. Small green squares are seismic stations used in receiver functions study in Ben-Mansour *et al.* (2018).

a small crack aspect ratio can increase the V_P/V_S ratio, large crack aspect ratio can decrease the V_P/V_S ratio (e.g. Shearer 1988; Takei 2002; Lin & Shearer 2009). Although it is difficult to pinpoint the exact rock units and physical parameters that govern the V_P/V_S ratio in Jektvik and Steigen, we speculate that fluids are present at the seismogenic depth in this region given the propensity for seismic swarms.

In case of ambiguity in the seismic velocity models, additional complementary constraints can be provided by electrical resistivity images. A recent magnetotelluric survey across Northern Norway and Sweden shows the presence of a large crustal conductive anomaly beneath Nordland (Cherevatova *et al.* 2015). They suggest the possibility of water infiltration through shear zones, for example Sagfjord shear zone. Some of the conductive anomalies are located near the high V_P/V_S ratio (Steigen region). From observations in active fault regions, low resistivity anomaly is often associated with the presence of fluid within the fault zones as observed in, for example San Andreas fault (Unsworth & Bedrosian 2004), and Kachchh rift (Kumar *et al.* 2017).

Along the Vestfjorden basin, we observe low V_P and high V_P/V_S ratio (∼1.81) (anomaly V in Sections C–C' and D–D'). This basin is filled with Mesozoic sediments (Olesen *et al.* 2002), and several normal faults that formed during the rifting processes are identified from geophysical methods (Olesen *et al.* 2002; Tsikalas *et al.* 2005). The combination of sedimentary basin and fault zones in the Vestfjorden basin is likely to reduce the V_P, and increase the V_P/V_S ratio slightly.

The most prominent feature of the middle and lower crust is the high V_P/V_S ratio (up to ≈1.85) (anomalies VI and VII in Fig. 7). Anomaly VI is most prominent in Sections E–E' and F–F'. Anomaly VI can be possibly attributed to the rock composition rather than the existence of fluid, because it is accompanied by slightly elevated V_P. Anomaly VII, located near the Moho step, is a result of increasing V_P. Anomalies VI and VII possibly indicate mafic rock composition, which is also found in the lower crust offshore Lofoten by Avedik *et al.* (1984) and Breivik *et al.* (2017), and along the mid Norwegian margin (Mjelde *et al.* 2016). The high-velocity body found in the lower crust along the Norwegian margin can be interpreted as the Eocene magmatic intrusions or the Caledonian eclogites (Mjelde *et al.* 2016).

7.3 The causes of intraplate seismicity in the coastal area of Nordland

Earthquakes in Nordland predominantly occur offshore along the shelf edge and onshore in the coastal area (see Fig. 9). A small number of earthquakes are also observed along the Lofoten-Vesterålen islands. The earthquake mechanisms vary from thrust faulting along the shelf edge (somewhat poorly resolved) to normal faulting along the coast. Our focal mechanisms show normal and oblique-normal solutions for events along the mainland coastal area. We do not have reliable solution for the Steigen swarm due to limited number of stations during the 2008–2009 period. For Jetvik, we obtained 12 focal mechanisms which are normal or slightly oblique-normal. The plot of *P*- and *T*-axes in Fig. 9 indicates coast perpendicular extension, which matches previous observations (Hicks *et al.* 2000b; Janutyte *et al.* 2017b). Further to the east, outside of the study area, the stress regime tends to be compressive as implied by focal mechanism studies of earthquakes in Northern Sweden (e.g. Arvidsson 1996; Lindblom 2011).

The local stress along the coast of Nordland is the opposite of what is expected from the mid Atlantic ridge push. It has been suggested that the local stress effects in Nordland, for example GIA, sedimentary loading, topography and lateral variation within the lithosphere (e.g. Fejerskov & Lindholm 2000; Bungum *et al.* 2010; Keiding *et al.* 2015), are strong enough to overcome the regional stress. The assumption is that the state of stress in the crust leads to reactivation of pre-existing faults (Atakan *et al.* 1994; Bungum *et al.* 2010). Here we attempt to combines our new result with previous constraints to identify the primary stress mechanisms in the Nordland region (Fig. 11).

Mass redistribution and respective isostatic adjustment, either due to sediment redistribution or ice removal result in flexural stress in the region. The high lateral uplift gradient along the coast of Nordland shown by Keiding *et al.* (2015) is possibly related to the effects of the flexural stress. The deglaciation process caused rapid erosion with a high rate of removal, along the coast of Nordland and Lofoten (Riis 1996), and deposition of thick sedimentary layers offshore, in particular the Naust formation. This process is suggested as a cause of local subsidence and uplift along the coast, and a significant contributor to the local stress regime (e.g. Redfield & Osmundsen

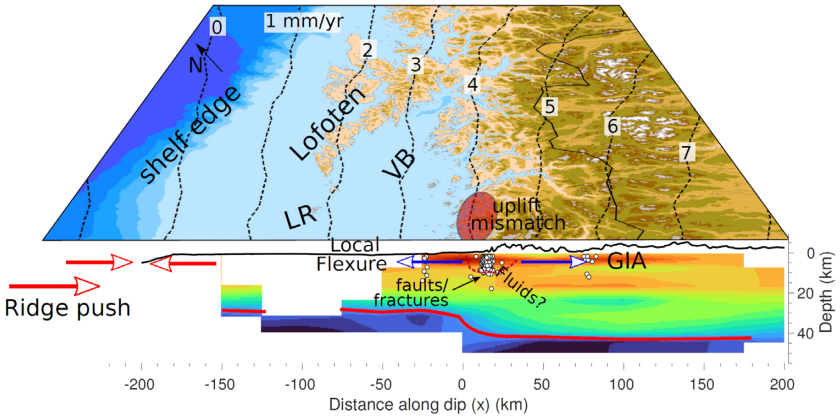

Figure 11. Sketch of the state of crustal stress in Nordland, overlain on the the V_P model crossing the Jektvik area (extended E–E' section) (see Fig. 7 for the V_P colorscale). Red line is the Moho surface derived in this study. Red and blue arrows represent compressive and extensional regimes. White open circles are the earthquake hypocentres. The uplift rate contours from Vestøl *et al.* (2019) are shown as dashed black lines. Approximate area where the largest misfit between GNSS and the GIA uplift reported by Kierulf (2017) is shown as a red ellipse. See Fig. 2 for the bathymetry scale.

2014; Gradmann *et al.* 2018). However, the contribution of this sedimentation and GIA to the present day stress in the region is not well understood. Furthermore, Kierulf (2017) showed a discrepancy in the coast of Nordland between the uplift rate derived using GNSS observations and that derived using a best-fitting GIA model. Our 3-D velocity model can help to improve previous GIA and stress modelling efforts in Nordland.

Another possible contributor to an extensional stress regime is the gravitational potential energy (GPE) stress that arises from density differences within the lithosphere, for example crustal thickness difference, as well as topographical effect (Pascal & Cloetingh 2009). The seismicity in Nordland concentrates along the coast, which coincides with the location of the Moho step. We speculate that the 10–15 km difference of continental crust thickness affects the local stress via GPE. Pascal & Cloetingh (2009) modelled the GPE stress in southern Norway, which is mainly caused by lithosperic density variation, crustal thickness and topography. They suggested that thicker crust and higher topography in southern Norway have a significant contribution on the extension in the onshore region and compression in the coastal and offshore domains. The setting in Nordland is similar, which makes GPE a plausible factor that can influence the crustal stress. However, further modelling is needed to verify how significant their contribution is to the local crustal stress.

As discussed in the previous section, our results suggest the presence of water in the upper crust, near the locations of the Jektvik ans Steigen swarms. Various observations have pointed to the importance of water in intraplate seismic swarm generation, for example in West Bohemia/Vogtland (Mousavi *et al.* 2015) and Kachchh rift (Kumar *et al.* 2017). There is no evidence for water migration from the deeper crust or mantle in this region. Alternatively, several studies have suggested that rainfall and surface water can trigger shallow seismicity (e.g. Hainzl *et al.* 2006; Bisrat *et al.* 2012; Craig *et al.* 2017), including in Nordland (Maystrenko *et al.* 2020a). However, in case of Nordland, this relation still needs to be verified with stress or hydrological modelling.

Whereas there may be explanations for the deviation from the regional compressive stress field, it is unclear how the system has changed with time and why the Nordland region remains critically stressed and thus near extensional failure. The effects of GIA may have resulted in an extensional setting after glaciation. The ridge push remains practically constant for the time frame considered here and the tectonic processes that affected the crust and formed structures such as the Moho step, have not been active for several tens of millions of years. Yet, the Nordland region is seismically active in a manner that contrasts with what is expected from the regional stress field. It is possible that the erosion remains active and keeps the differential stresses high. The presence of fluids as suggested by our tomography model may play an important role in bringing the system to failure by reducing friction along the faults. In Norway, neither of these processes is unique to Nordland, but perhaps this combination can explain the high seismic activity of the area.

8 CONCLUSIONS

3-D V_P and V_P/V_S ratio models of the Nordland region were developed using seismic traveltime tomography. These models then served as a basis to build a new seismicity catalogue and compute focal mechanisms. Our results provide important new insight into the crustal structure of the region and the causes of intraplate seismicity in Nordland.

The crustal thickness and seismic velocities inferred from our models were found to vary considerably across the study area. Below the Lofoten-Vesterålen islands, crustal thicknesses range from ∼27 km in the south to ∼35 km in the north. Between southern Lofoten and the mainland area, the crust thickens rather abruptly over a lateral distance of only ∼25 km, forming a Moho step that runs parallel to the coast. The crust in the mainland part of Nordland is thicker, ranging from 40 to 47 km. The tomography images show low V_P and variable V_P/V_S ratio anomalies in the vicinity of the Steigen and Jektvik swarms, possibly indicating the existence of fractures and fluids in the upper crust.

To investigate the causes of seismicity, we considered our results in the context of local and regional stresses. In the coastal part of mainland Nordland, the stress regime exhibits coast-perpendicular extension, in contrast to the prevalent regional compressive stresses. We propose that the shallow crustal stress in Nordland is dominated by flexural stress due to sediment redistribution and GIA. The high seismicity area along the coast of Nordland coincides with the location of the Moho step. This is a possible indication that GPE can also contribute to the local stress here. Deformation localizes within pre-existing fault zones, which in some cases have been weakened by

fluids. This set of conditions leads to the occurrence of earthquakes and is favourable to the development of seismic swarms.

FUNDING

The study was supported by funding from the Research Council of Norway for the project 'IPSIN - Intraplate Seismicity in India and Norway: Distribution, properties and causes' (project 248815).

ACKNOWLEDGMENTS

We thank Richard England and Victoria Lane at SEIS-UK for providing us the seismic data for SCANLIPS3D (ZR) network. We acknowledge the operators of permanent and temporary seismic networks used in this study: NNSN (NS), NORSAR stations (NO), SNSN (UP), FNSN (HE), NEONOR2 (2G), ScanArray (1G), Scanlips2 (Y1) and Scanlips3D (ZR). The authors grateful for helpful discussions with Thomas Theunissen and Jhon Muñoz-Barrera of University of Bergen. We thank the editor Ian Bastow, an anonymous reviewer and Trine Dahl-Jensen for constructive comments on the manuscript.

DATA AVAILABILITY

Earthquake data catalogue from the Norwegian National Seismic Network (NNSN) (Ottemöller et al. 2018) with additional new phase picks processed in this study is available at NNSN webpage (https://nnsn.geo.uib.no/nnsn/#/data/events/bulletins). Seismic data from NNSN (network code: NS, Ottemöller *et al.* 2021), Norsar stations (NO, Schweitzer *et al.* 2021) and Neonor2 (2G, Michálek *et al.* 2018) are available at UiB-Norsar European Integrated Data Archive (EIDA) Node webpage (https://nnsn.geo.uib.no/nnsn/#/data/waveforms/access). Seismic data from SNSN (UP, Lund *et al.* 2021), FNSN (HE) (Veikkolainen *et al.* 2021) and ScanArray (1G, Thybo *et al.* 2021) networks are archived at the Observatories and Research Facilities for European Seismology (ORFEUS) EIDA (http://www.orfeus-eu.org/data/eida/, Strollo *et al.* 2021). Seismic data for Scanlips2 (Y1, https://www.fdsn.org/networks/detail/Y1_2007/) and Scanlips3D (ZR, England *et al.* 2016) network are archived at the Incorporated Research Institutions for Seismology (IRIS) Data Management Center (DMC, http://ds.iris.edu/ds/nodes/dmc/). Earthquake data were processed using Seisan earthquake analysis software (Havskov & Ottemöller 1999; Havskov et al. 2020) (http://seisan.info/). Figures in this paper were created using Generic Mapping Tools (Wessel *et al.* 2013), Matlab (https://www.mathworks.com/products/matlab.html), M_Map Matlab package (Pawlowicz 2020) (https://www.eoas.ubc.ca/~rich/map.html) and Inkscape, a vector graphics editor (https://inkscape.org/). The hypocentre locations, focal mechanisms, velocity models and Moho surface depth generated in this study is available at Zenodo (https://doi.org/10.5281/zenodo.5778841).

REFERENCES

Altamimi, Z., Rebischung, P., Métivier, L. & Collilieux, X., 2016. ITRF2014: a new release of the International Terrestrial Reference Frame modeling nonlinear station motions, *J. geophys. Res.,* **121**(8), 6109–6131.

Arvidsson, R., 1996. Fennoscandian earthquakes: whole crustal rupturing related to postglacial rebound, *Science,* **274**(5288), 744–746.

Atakan, K., Lindholm, C.D. & Havskov, J., 1994. Earthquake swarm in Steigen, northern Norway: an unusual example of intraplate seismicity, *Terra Nova,* **6**(2), 180–194.

Avedik, F., Berendsen, D., Fucke, H., Goldflam, S. & Hirschleber, H., 1984. Seismic investigations along the Scandinavian Blue Norma profile, *Ann. Geophys.,* **2**(5), 571–577.

Ben-Mansour, W., England, R.W., Fishwick, S. & Moorkamp, M., 2018. Crustal properties of the northern Scandinavian mountains and Fennoscandian shield from analysis of teleseismic receiver functions, *Geophys. J. Int.,* **214**(1), 386–401.

Bisrat, S., DeShon, H.R. & Rowe, C., 2012. Microseismic swarm activity in the New Madrid Seismic Zone, *Bull. seism. Soc. Am.,* **102**(3), 1167–1178.

Bleibinhaus, F., 2003. 3D Simultaneous Refraction and Reflection Seismic Travel Time Tomography and Application to Deep Seismic TRANSALP Wide-Angle Data, *PhD dissertation*, Ludwig-Maximilians-Universität, München, Germany.

Bleibinhaus, F. & Gebrande, H., 2006. Crustal structure of the Eastern Alps along the TRANSALP profile from wide-angle seismic tomography, *Tectonophysics,* **414**(1), 51–69.

Bleibinhaus, F. & Hilberg, S., 2012. Shape and structure of the Salzach Valley, Austria, from seismic traveltime tomography and full waveform inversion, *Geophys. J. Int.,* **189**(3), 1701–1716.

Brantut, N. & David, E.C., 2018. Influence of fluids on VP/VS ratio: increase or decrease? *Geophys. J. Int.,* **216**(3), 2037–2043.

Breivik, A.J., Faleide, J.I., Mjelde, R., Flueh, E.R. & Murai, Y., 2017. A new tectono-magmatic model for the Lofoten/Vesterålen Margin at the outer limit of the Iceland Plume influence, *Tectonophysics,* **718,** 25–44.

Breivik, A.J., Faleide, J.I., Mjelde, R., Flueh, E.R. & Murai, Y., 2020. Crustal structure and erosion of the Lofoten/Vesterålen shelf, northern Norwegian margin, *Tectonophysics,* **776,** doi:10.1016/j.tecto.2020.228318.

Brönner, M., Gernigon, L. & Nasuti, A., 2013. Lofoten-Vestfjorden Aeromagnetic Survey 2011 – LOVAS-11 Acquisition, Processing and Interpretation report.

Bungum, H., Alsaker, A., Kvamme, L.B. & Hansen, R.A., 1991. Seismicity and seismotectonics of Norway and nearby continental shelf areas, *J. geophys. Res.,* **96**(B2), 2249–2265.

Bungum, H., Hokland, B.K., Husebye, E.S. & Ringdal, F., 1979. An exceptional intraplate earthquake sequence in Meløy, Northern Norway, *Nature,* **280,** 32–35.

Bungum, H. & Olesen, O., 2005. The 31st of August 1819 Lurøy earthquake revisited, *Norweg. J. Geol.,* (85), 245–252.

Bungum, H., Olesen, O., Pascal, C., Gibbons, S., Lindholm, C. & Vestøl, O., 2010. To what extent is the present seismicity of Norway driven by post-glacial rebound? *J. Geol. Soc.,* **167**(2), 373–384.

Bungum, H., Vaage, S. & Husebye, E.S., 1982. The Meløy earthquake sequence, northern Norway: source parameters and their scaling relations, *Bull. seism. Soc. Am.,* **72**(1), 197–206.

Cherevatova, M. *et al.*, 2015. Magnetotelluric array data analysis from northwest Fennoscandia, *Tectonophysics,* **653,** 1–19.

Corfu, F., Andersen, T.B. & Gasser, D., 2014. The Scandinavian Caledonides: main features, conceptual advances and critical questions, *Geol. Soc., Lond., Spec. Publ.,* **390**(1), 9–43.

Craig, T.J., Chanard, K. & Calais, E., 2017. Hydrologically-driven crustal stresses and seismicity in the New Madrid Seismic Zone, *Nat. Commun.,* **8,** doi:10.1038/s41467-017-01696-w.

Demuth, A., Ottemöller, L. & Keers, H., 2019. QLg wave tomography beneath Norway, *J. Seismol.,* **23,** 151–164.

Diehl, T., Husen, S., Kissling, E. & Deichmann, N., 2009. High-resolution 3-D P-wave model of the Alpine crust, *Geophys. J. Int.,* **179**(2), 1133–1147.

Ekström, G., Nettles, M. & Dziewoński, A., 2012. The global CMT project 2004–2010: centroid-moment tensors for 13,017 earthquakes, *Phys. Earth planet. Inter.,* **200–201,** 1–9.

Eldholm, O. & Grue, K., 1994. North Atlantic volcanic margins: dimensions and production rates, *J. geophys. Res.,* **99**(B2), 2955–2968.

Ellsworth, W.L., 1978. Three-dimensional structure of the crust and mantle beneath the island of Hawaii, *PhD dissertation*, Dept. of Earth and Planetary Sciences, Massachusetts Institute of Technology, Cambridge, MA.

England, R.W., Ebbing, J. & Ben-Mansour, W., 2016. SCANLIPS3D: SCANdinavian LIthosphere P and S wave experiment

3D instrument loan report, NERC Geophysical Equipment Facility, http://gef.nerc.ac.uk/reports.php.

Evans, D., McGiveron, S., McNeill, A., Harrison, Z., Østmo, S. & Wild, J., 2000. Plio-Pleistocene deposits on the mid-Norwegian margin and their implications for late Cenozoic uplift of the Norwegian mainland, *Global Planet. Change,* **24**(3), 233–237.

Evans, J., Eberhart-Phillips, D. & Thurber, C., 1994. User's manual for SIMULPS12 for imaging Vp and Vp/Vs: a derivative of the Thurber tomographic inversion SIMUL3 for local earthquakes and explosions, U.S. Geological Survey Open File Report 94–431.

Faleide, J.I., Tsikalas, F., Breivik, A.J., Mjelde, R., Ritzmann, O., Øyvind, E., Wilson, J. & Eldholm, O., 2008. Structure and evolution of the continental margin off Norway and the Barents Sea, *Episodes,* **31**(1), 82–91.

Fejerskov, M. & Lindholm, C., 2000. Crustal stress in and around Norway: an evaluation of stress-generating mechanisms, *Geol. Soc., Lond., Spec. Publ.,* **167**(1), 451–467.

Fjeldskaar, W., Lindholm, C., Dehls, J.F. & Fjeldskaar, I., 2000. Postglacial uplift, neotectonics and seismicity in Fennoscandia, *Quater. Sci. Rev.,* **19**(14), 1413–1422.

Fossen, H., 2010. Extensional tectonics in the North Atlantic Caledonides: a regional view, in *Continental Tectonics and Mountain Building: The Legacy of Peach and Horne,* Geological Society of London.

Geological Survey of Norway, 2011. *Nasjonal berggrunnsdatabase*.

Gradmann, S. & Ebbing, J., 2015. Large-scale gravity anomaly in northern Norway: tectonic implications of shallow or deep source depth and a possible conjugate in northeast Greenland, *Geophys. J. Int.,* **203**(3), 2070–2088.

Gradmann, S., Haase, C. & Ebbing, J., 2017. Isostasy as a tool to validate interpretations of regional geophysical datasets – application to the mid-Norwegian continental margin, *Geol. Soc., Lond., Spec. Publ.,* **447**(1), 279–297.

Gradmann, S., Olesen, O., Keiding, M. & Maystrenko, Y., 2018. The Regional 3D Stress Field of Nordland, Northern Norway - Insights from Numerical Modelling, chap. Neotectonics in Nordland - Implications for petroleum exploration (NEONOR2), Geological Survey of Norway, Trondheim.

Hainzl, S., Kraft, T., Wassermann, J., Igel, H. & Schmedes, E., 2006. Evidence for rainfall-triggered earthquake activity, *Geophys. Res. Lett.,* **33**(19),.

Halpaap, F., Rondenay, S. & Ottemöller, L., 2018. Seismicity, deformation, and metamorphism in the Western Hellenic Subduction Zone: new constraints from tomography, *J. geophys. Res.,* **123**(4), 3000–3026.

Halpaap, F., Rondenay, S., Perrin, A., Goes, S., Ottemöller, L., Austrheim, H., Shaw, R. & Eeken, T., 2019. Earthquakes track subduction fluids from slab source to mantle wedge sink, *Sci. Adv.,* **5**(4), doi:10.1126/sciadv.aav7369.

Hardebeck, J.L. & Shearer, P.M., 2002. A new method for determining first-motion focal mechanisms, *Bull. seism. Soc. Am.,* **92**(6), 2264–2276.

Havskov, J. & Bungum, H., 1987. Source parameters for earthquakes in the northern North Sea, *Norsk Geologisk Tidsskrift,* **67,** 51–58.

Havskov, J. & Ottemoller, L., 1999. SeisAn earthquake analysis software, *Seismol. Res. Lett.,* **70**(5), 532–534.

Havskov, J. & Ottemöller, L., 2010. *Routine Data Processing in Earthquake Seismology: With Sample Data, Exercises and Software,* Springer.

Havskov, J., Voss, P.H. & Ottemöller, L., 2020. Seismological observatory software: 30 Yr of SEISAN, *Seismol. Res. Lett.,* **91**(3), 1846–1852.

Hicks, E.C., Bungum, H. & Lindholm, C.D., 2000a. Seismic activity, inferred crustal stresses and seismotectonics in the Rana region, Northern Norway, *Quater. Sci. Rev.,* **19**(14), 1423–1436.

Hicks, E.C., Bungum, H. & Lindholm, C.D., 2000b. Stress inversion of earthquake focal mechanism solutions from onshore and offshore Norway, *Norsk Geologisk Tidsskrift,* **80**(4), 235–250.

Horni, J.Á. *et al.*, 2017. Regional distribution of volcanism within the North Atlantic Igneous Province, *Geol. Soc., Lond., Spec. Publ.,* **447**(1), 105–125.

Husen, S., Kissling, E. & Clinton, J., 2011. Local and regional minimum 1D models for earthquake location and data quality assessment in complex tectonic regions: application to Switzerland, *Swiss J. Geosci.,* **104,** 455–469.

Husen, S., Kissling, E., Deichmann, N., Wiemer, S., Giardini, D. & Baer, M., 2003. Probabilistic earthquake location in complex three-dimensional velocity models: application to Switzerland, *J. geophys. Res.,* **108**(B2), doi:10.1029/2002JB001778.

Janutyte, I., Lindholm, C. & Olesen, O., 2017a. Relation between seismicity and tectonic structures offshore and onshore Nordland, northern Norway, *Norweg. J. Geol.,* **97**(3), 211–225.

Janutyte, I., Lindholm, C. & Olesen, O., 2017b. Earthquake source mechanisms in onshore and offshore Nordland, northern Norway, *Norweg. J. Geol.,* **97**(3), 227–239.

Keiding, M., Kreemer, C., Lindholm, C., Gradmann, S., Olesen, O. & Kierulf, H., 2015. A comparison of strain rates and seismicity for Fennoscandia: depth dependency of deformation from glacial isostatic adjustment, *Geophys. J. Int.,* **202**(2), 1021–1028.

Kierulf, H.P., 2017. Analysis strategies for combining continuous and episodic GNSS for studies of neo-tectonics in Northern-Norway, *J. Geodyn.,* **109,** 32–40.

Kissling, E., 1995. Velest user's guide, Institute of Geophysics, ETH Zuerich, pp. 1–26.

Kissling, E., Ellsworth, W.L., Eberhart-Phillips, D. & Kradolfer, U., 1994. Initial reference models in local earthquake tomography, *J. geophys. Res.,* **99**(B10), 19 635–19 646.

Klein, F., 2002. User's Guide to HYPOINVERSE-2000, a Fortran program to solve for earthquake locations and magnitudes, U.S. Geological Survey Open File Report 02–171.

Koulakov, I., 2009. Out-of-network events can be of great importance for improving rResults of local earthquake tomography, *Bull. seism. Soc. Am.,* **99**(4), 2556–2563.

Koulakov, I., Maksotova, G., Mukhopadhyay, S., Raoof, J., Kayal, J.R., Jakovlev, A. & Vasilevsky, A., 2015. Variations of the crustal thickness in Nepal Himalayas based on tomographic inversion of regional earthquake data, *Solid Earth,* **6**(1), 207–216.

Kumar, G.P., Mahesh, P., Nagar, M., Mahender, E., Kumar, V., Mohan, K. & Ravi Kumar, M., 2017. Role of deep crustal fluids in the genesis of intraplate earthquakes in the Kachchh region, northwestern India, *Geophys. Res. Lett.,* **44**(9), 4054–4063.

Kuo-Chen, H., Wu, F.T., Jenkins, D.M., Mechie, J., Roecker, S.W., Wang, C.-Y. & Huang, B.-S., 2012. Seismic evidence for the - quartz transition beneath Taiwan from Vp/Vs tomography, *Geophys. Res. Lett.,* **39**(22), doi:10.1029/2012GL053649.

Lange, D., Tilmann, F., Henstock, T., Rietbrock, A., Natawidjaja, D. & Kopp, H., 2018. Structure of the central Sumatran subduction zone revealed by local earthquake travel-time tomography using an amphibious network, *Solid Earth,* **9**(4), 1035–1049.

Laske, G., Masters, G., Ma, Z. & Pasyanos, M., 2013. Update on CRUST1.0 - a 1-degree Global Model of Earth's Crust, in *EGU General Assembly Conference Abstracts,* Vol. **15,** pp. EGU2013–2658.

Leónios, S. *et al.*, 2021. 3D local earthquake tomography of the Ecuadorian margin in the source area of the 2016 Mw 7.8 Pedernales earthquake, *J. geophys. Res.,* **126**(3), e2020JB020701, doi:10.1029/2020JB020701.

Lienert, B.R. & Havskov, J., 1995. A computer program for locating earthquakes both locally and globally, *Seismol. Res. Lett.,* **66**(5), 26–36.

Lin, G. & Shearer, P.M., 2009. Evidence for water-filled cracks in earthquake source regions, *Geophys. Res. Lett.,* **36**(17), doi:10.1029/2009GL039098.

Lindblom, E., 2011. Microearthquake study of end-glacial faults in Northern Sweden, *PhD dissertation*, Uppsala University.

Lund, B., Schmidt, P., Hossein Shomali, Z. & Roth, M., 2021. The Modern Swedish National Seismic Network: two decades of intraplate microseismic observation, *Seismol. Res. Lett.,* **92**(3), 1747–1758.

Måntyniemi, P.B., Sørensen, M.B., Tatevossian, T.N., Tatevossian, R.E. & Lund, B., 2020. A reappraisal of the Lurøy, Norway, earthquake of 31 August 1819, *Seismol. Res. Lett.,* **91**(5), doi:10.1785/0220190363.

Mauerberger, A., Maupin, V., Sadeghisorkhani, H., Gudmundsson, O. & Tilmann, F., 2020. Scandinavian lithosphere structure derived from surface waves and ambient noise, in *EGU General Assembly Conference Abstracts,* pp. EGU2020–8366.

Maystrenko, Y., Brönner, M., Olesen, O., Saloranta, T.M. & Slagstad, T., 2020a. Atmospheric precipitation and anomalous upper mantle in relation to intraplate seismicity in Norway, *Tectonics,* **39**(9), e2020TC006070, doi:10.1029/2020TC006070.

Maystrenko, Y., Gernigon, L. & Olesen, O., 2020b. Comment on "Crustal structure and erosion of the Lofoten/Vesterålen shelf, northern Norwegian margin. Tectonophysics 776, 228318" by A.J. Breivik, J.I. Faleide, R. Mjelde, E.R. Flueh, Y. Murai, *Tectonophysics,* **793,** 228605, doi:10.1016/j.tecto.2020.228605.

Maystrenko, Y., Olesen, O., Gernigon, L. & Gradmann, S., 2017. Deep structure of the Lofoten-Vesterålen segment of the Mid-Norwegian continental margin and adjacent areas derived from 3-D density modeling, *J. geophys. Res.,* **122**(2), 1402–1433.

Michálek, J., Tjåland, N., Drottning, A., Strømme, M.L., Storheim, B.M., Rondenay, S. & Ottemöller, L., 2018. Report on seismic observations within the NEONOR2 project in the Nordland region, Norway (Aug. 2013 - May 2016), chap. Neotectonics in Nordland - Implications for petroleum exploration (NEONOR2), Geological Survey of Norway, Trondheim.

Midzi, V., Saunders, I., Brandt, M. B.C. & Molea, T., 2010. 1-D Velocity Model for Use by the SANSN in Earthquake Location, *Seismol. Res. Lett.,* **81**(3), 460–466.

Mjelde, R. *et al.*, 1998. Crustal structure of the northern part of the Vøring Basin, mid-Norway margin, from wide-angle seismic and gravity data, *Tectonophysics,* **293**(3), 175–205.

Mjelde, R., Goncharov, A. & Müller, R.D., 2013. The Moho: boundary above upper mantle peridotites or lower crustal eclogites? A global review and new interpretations for passive margins, *Tectonophysics,* **609,** 636–650.

Mjelde, R., Kvarven, T., Faleide, J.I. & Thybo, H., 2016. Lower crustal high-velocity bodies along North Atlantic passive margins, and their link to Caledonian suture zone eclogites and Early Cenozoic magmatism, *Tectonophysics,* **670,** 16–29.

Mjelde, R. & Sellevoll, M.A., 1993. Possible shallow crustal shear wave anisotropy off Lofoten, Norway, inferred from three-component ocean-bottom seismographs, *Geophys. J. Int.,* **115**(1), 159–167.

Mjelde, R., Sellevoll, M.A., Shimamura, H., Iwasaki, T. & Kanazawa, T., 1993. Crustal structure beneath Lofoten, N. Norway, from vertical incidence and wide-angle seismic data, *Geophys. J. Int.,* **114**(1), 116–126.

Mousavi, S., Bauer, K., Korn, M. & Hejrani, B., 2015. Seismic tomography reveals a mid-crustal intrusive body, fluid pathways and their relation to the earthquake swarms in West Bohemia/Vogtland, *Geophys. J. Int.,* **203**(2), 1113–1127.

Muir-Wood, R., 1989. The Scandinavian earthquakes of 22 December 1759 and 31 August 1819, *Disasters,* **12**(3), 223–236.

Newrkla, K.,Shiddiqi, H.A.,Jerkins, A.E.,Keers, H.& Ottemöller, L.,2019.Implications of 3D Seismic Raytracing on Focal Mechanism Determination *Bull. Seism. Soc. Am.,* **109**(6).

Olesen, O. *et al.*, 2010. Gravity anomaly map, Norway and adjacent areas; Scale 1:3 mill, Geological Survey of Norway.

Olesen, O., Lundin, E., Nordgulen, O., Osmundsen, P., Skilbrei, J., Smethurst, M., Solli, A., Bugge, T. & Fichler, C., 2002. Bridging the gap between onshore and offshore geology in Nordland, northern Norway, *Norweg. J. Geol.,* **82**(4), 243–262.

Ottemöller, L., Michalek, J., Christensen, J., Baadshaug, U., Halpaap, F., Natvik, y., Kværna, T. & Oye, V., 2021. UiB-NORSAR EIDA node: integration of seismological data in Norway, *Seismol. Res. Lett.,* **92**(3), 1491–1500.

Ottemöller, L. & Midzi, V., 2003. The crustal structure of Norway from inversion of teleseismic receiver functions, *J. Seismol.,* **7,** 35–48.

Ottemöller , L., Strømme , M.L. & Storheim, B.M.,.2018,Seismic monitoring and data processing at the Norwegian National Seismic Network , in*Summary of the Bulletin of the International Seismological Centre 2015 January-June,***51**(1), ed.Lieser , K.,Harris , J.& Storchak , D.,International Seismological Centre.

Pascal, C. & Cloetingh, S.A., 2009. Gravitational potential stresses and stress field of passive continental margins: insights from the south-Norway shelf, *Earth planet. Sci. Lett.,* **277**(3), 464–473.

Pawlowicz, R., 2020. M_Map: A mapping package for MATLAB(Computer software), https://www.eoas.ubc.ca/~rich/map.html.

Redfield, T.F. & Osmundsen, P.T., 2014. Some remarks on the earthquakes of Fennoscandia: a conceptual seismological model drawn from the perspective of hyperextension, *Norweg. J. Geol.,* **9,** 233–262.

Rietbrock, A., 1996. Entwicklung eines Programmsystems zur konsistenten Auswertung großer seismologischer Datensätze mit Anwendung auf die Untersuchung der Absorptionsstruktur der Loma-Prieta-Region, Kalifornien, *PhD dissertation*, Ludwig-Maximilians-Universität, München, Germany.

Riis, F., 1996. Quantification of Cenozoic vertical movements of Scandinavia by correlation of morphological surfaces with offshore data, *Global planet. Change,* **12**(1), 331–357.

Rise, L., Ottesen, D., Berg, K. & Lundin, E., 2005. Large-scale development of the mid-Norwegian margin during the last 3 million years, *Mar. Petrol. Geol.,* **22**(1), 33–44.

Schulte, S.M. & Mooney, W.D., 2005. An updated global earthquake catalogue for stable continental regions: reassessing the correlation with ancient rifts, *Geophys. J. Int.,* **161**(3), 707–721.

Schweitzer, J., Köhler, A. & Christensen, J.M., 2021. Development of the NORSAR network over the last 50 Yr, *Seismol. Res. Lett.,* **92**(3), 1501–1511.

Sellevoll, M., 1983. A study of the earth's crust in the island area of Lofoten-Vesterålen, Northern Norway, *Norsk Geologisk Tidsskrift,* **380,** 235–243.

Shearer, P.M., 1988. Cracked media, Poisson's ratio and the structure of the upper oceanic crust, *Geophys. J. Int.,* **92**(2), 357–362.

Shiddiqi, H.A., Tun, P.P. & Ottemöller, L., 2019. Minimum 1D velocity model and local magnitude scale for Myanmar, *Seismol. Res. Lett.,* **90**(5), 1923–1936.

Snoke, J.A., 2003. FOCMEC: focal mechanism determinations, in *International Handbook of Earthquake and Engineering Seismology,* Chapter 85.12, pp. 1629–1630, eds Lee, W., Jennings, P., Kisslinger, C. & Kanamori, H., Academic Press.

Steffen, H. & Kaufmann, G., 2005. Glacial isostatic adjustment of Scandinavia and northwestern Europe and the radial viscosity structure of the Earth's mantle, *Geophys. J. Int.,* **163**(2), 801–812.

Strollo, A. *et al.*, 2021. EIDA: the European integrated data archive and service infrastructure within ORFEUS, *Seismol. Res. Lett.,* **92**(3), 1788–1795.

Takei, Y., 2002. Effect of pore geometry on VP/VS: From equilibrium geometry to crack, *J. geophys. Res.,* **107**(B2), ECV6–1-ECV6-12.

Takemura, S.,Shiomi, K.,Kimura, T.& Saito , T.,2016.Systematic difference between first-motion and waveform-inversion solutions for shallow offshore earthquakes due to a low-angle dipping slab,*Earth Planet Sp.* **68**(149) 1–8.

Thurber, C.H., 1983. Earthquake locations and three-dimensional crustal structure in the Coyote Lake Area, central California, *J. geophys. Res.,* **88**(B10), 8226–8236.

Thurber, C.H. & Eberhart-Phillips, D., 1999. Local earthquake tomography with flexible gridding, *Comp. Geosci.,* **25**(7), 809–818.

Thybo, H. *et al.*, 2021. ScanArray—a broadband seismological experiment in the Baltic Shield, *Seismol. Res. Lett.,* **92**(5), 2811–2823.

Tozer, B., Sandwell, D.T., Smith, W.H.F., Olson, C., Beale, J.R. & Wessel, P., 2019. Global bathymetry and topography at 15 arc sec: SRTM15+, *Earth Space Sci.,* **6**(10), 1847–1864.

Tsikalas, F., Eldholm, O. & Faleide, J.I., 2005. Crustal structure of the Lofoten–Vesterålen continental margin, off Norway, *Tectonophysics,* **404**(3), 151–174.

Tsikalas, F., Faleide, J.I. & Eldholm, O., 2001. Lateral variations in tectonomagmatic style along the Lofoten–Vesterålen volcanic margin off Norway, *Mar. Petrol. Geol.,* **18**(7), 807–832.

Unsworth, M. & Bedrosian, P., 2004. Electrical Resistivity structure at the SAFOD site from magnetotelluiric exploration, *Geophys. Res. Lett,* **31,** 12–5.

Unsworth, M. & Rondenay, S., 2013. *Mapping the Distribution of Fluids in the Crust and Lithospheric Mantle Utilizing Geophysical Methods,* pp. 535–598, Springer Berlin Heidelberg.

Veikkolainen, T. *et al.*, 2021. The Finnish National Seismic Network: toward fully automated analysis of low-magnitude seismic events, *Seismol. Res. Lett.,* **92**(3), 1581–1591.

Vestøl, O., Ågren, J., Steffen, H., Kierulf, H. & Tarasov, L., 2019. NKG2016LU: a new land uplift model for Fennoscandia and the Baltic Region, *J. Geod.,* **93,** 1759–1779.

Wang, Q. & Ji, S., 2009. Poisson's ratios of crystalline rocks as a function of hydrostatic confining pressure, *J. geophys. Res.,* **114**(B9), doi:10.1029/2008JB006167.

Wessel, P., Smith, W. H.F., Scharroo, R., Luis, J. & Wobbe, F., 2013. Generic mapping tools: improved version released, *EOS, Trans. Am. Geophys. Un.,* **94**(45), 409–410.

Wright, C., 2008. Station corrections for the Kaapvaal seismic network: Statistical properties and relation to lithospheric structure, *Phys. Earth planet. Inter.,* **167**(1), 39–52.

Wu, P. & Hasegawa, H.S., 1996. Induced stresses and fault potential in eastern Canada due to a disc load: a preliminary analysis, *Geophys. J. Int.,* **125**(2), 415–430.

SUPPORTING INFORMATION

Supplementary data are available at *GJI* online.

Figure S1. Ray path distribution from NNSN data set (a) and ray path distribution from the final data set used in this study (b). Ray paths are shown as grey lines. Earthquake locations and stations are shown as circles coloured with depth and blue inverted triangles, respectively. Location of Kvannevann mine is shown as the black stars.

Figure S2. Final ray path distribution (blue lines) and fine inversion grid nodes (black circles) in map view as well as along strike and dip sections. The central coordinate ($X = 0$ km, $Y = 0$ km) of the tomography model (shown as the green star) is 67.5°N, and 14.5°E, and the coordinate system is rotated 35° clockwise. Stations are shown as red inverted triangles.

Figure S3. Moho step test showing the synthetic model (left-hand panel) and the inversion result (right-hand panel). The synthetic model is created by combining two 1-D V_P models with a shallower Moho in the west and a deeper Moho in the east. This test was performed to demonstrate that our inversion can actually recover the Moho step feature in Nordland. The hypocentres are shown as white circles. The solid red lines are the 'Moho velocity' contour ($V_P = 7.6$ km s^{-1}).

Figure S4. Smooth Moho test showing the synthetic model (left-hand panel) and the inversion result (right-hand panel). The synthetic model is created by using two 1-D V_P with smooth transition. This test aimed to demonstrate that the Moho step is not an artefact created by the inversion set-up. The hypocentres are shown as white circles. The solid red lines are the 'Moho velocity' contour ($V_P =$ 7.6 km s^{-1}).

Figure S5. Coast perpendicular cross-sections showing the ray path distribution (black dots) for observations used in the 3-D velocity inversion. Red lines are the contour of the 'Moho velocity' (V_P = 7.6 km s^{-1}). White circles represent the earthquake locations. Surface topography (with 4× vertical exaggeration) are also plotted on the top of each sections.

Figure S6. Synthetic test to evaluate whether the Moho step (black lines) creates an artificial anomaly or not. The test includes (a) constant V_P/V_S ratio with higher random noise, (b) low V_P/V_S ratio in the lower crust of the offshore and (c) high V_P/V_S ratio in the upper crust of the mainland area. This test shows that our inversion set-up does not create artificial anomaly near the Moho step.

Figure S7. 1-D V_P and V_S models derived using six starting models, which used three Moho depths: 35, 40 and 45 km. The preferred 1-D model is the Crust1.0 based model with 40 km Moho depth.

Figure S8. *P*-wave station delays for six 1-D velocity models in Fig. S7. All delays are relative to the reference station.

Figure S9. Comparison of hypocentres in Steigen area determined using four velocity model (1-D, 3-D coarse, 3-D medium and 3-D fine models).

Figure S10. Comparison of hypocentres in Jektvik area determined using four velocity model (1-D, 3-D coarse, 3-D medium and 3-D fine models).

Figure S11. V_P and V_P/V_S ratio for coast parallel cross-sections. Red lines are the contour of the 'Moho velocity' (V_P 7.6 km s^{-1}), and the dashed black lines is the Moho model compiled by Maystrenko *et al*. (2017). Hypocentre and stations are represented by white circles and black triangles, respectively. Surface topography (with 4× vertical exaggeration) are plotted on the top of each cross-section. The inversion grids are plotted in V_P/V_S ratio sections.

Figure S12. Horizontal slices for V_P and V_P/V_S ratio in the middle and lower crustal depth. Earthquakes and stations are shown as red circles and open inverted triangles.

Figure S13. Comparison between focal mechanism solutions computed using 1-D velocity model (left-hand panel) and solutions computed using 3-D velocity model. Nodal lines represent all possible solutions that fit with the observations. Position of polarities and amplitude ratios are plotted within the lower hemisphere projection. Compression and dilatation polarities are shown as open circles and open triangles, respectively, and amplitude ratios are plotted as H symbols.

Please note: Oxford University Press is not responsible for the content or functionality of any supporting materials supplied by the authors. Any queries (other than missing material) should be directed to the corresponding author for the paper.